Diffusion-Based MR Methods for Measuring Water Exchange

Diffusionsbaserade MR-metoder för mätning av vattenutbyte

Shan Cai

Supervisor : Alfredo Ordinola
Examiner : Dr. Evren Özarslan

Abstract

Measuring transmembrane water exchange can provide potential biomarkers for tumors and brain disorders. Diffusion Magnetic Resonance Imaging (dMRI) is a well-established tool that can non-invasively measure water exchange across cell membranes. Diffusion Exchange Spectroscopy (DEXSY) is one of the dMRI-based frameworks used to estimate exchange. DEXSY provides a detailed picture of multi-site exchange processes but requires a large quantity of data. Several models based on the DEXSY framework have been proposed to reduce the acquisition time. Filter Exchange Imaging (FEXI) and curvature models are two of them that only require certain samples of the DEXSY dataset. Diffusion-Exchange Weighted (DEW) Imaging model is another data reduction method accounting for restricted diffusion within cells and can use a specific subset of the DEXSY dataset to measure exchange. Furthermore, a more general expression of the DEXSY signal, referred to as the general model, can theoretically analyze the full space or reduced DEXSY datasets and estimate exchange. However, the results of the subsampling schemes and the data reduction models have not been compared to the full space estimation.

Therefore, this thesis aims to experimentally explore the feasibility of estimating exchange using these four models (the general, FEXI, curvature and DEW models) with the data acquired using a low-field benchtop MR scanner, and compare the estimates from the general model with different subsampling schemes and the data reduction models to the full space estimation. For this purpose, a double diffusion encoding (DDE) sequence was modified from an existing sequence on the benchtop MR scanner and a DEXSY experiment was conducted on this MR scanner and a yeast phantom to acquire a full space dataset. The exchange parameters estimated from the full space dataset using the general model were used as "ground truths" to evaluate the estimates from the reduced datasets analyzed using the general, FEXI and curvature models. Moreover, two alternative subsampling schemes named the shifted DEW and new trajectory schemes were proposed and employed to measure exchange.

The results indicate that all the methods except the curvature sampling scheme employed with both the general and curvature models provided comparable estimates to the "ground truths". The shifted DEW and new trajectory sampling schemes performed better over others in terms of consistency with the "ground truths" and low variations between voxels, suggesting the theoretical and experimental optimization of these two subsampling schemes can be further studied and developed.

Acknowledgments

First, I would like to thank my supervisor, Alfredo Ordinola, for his constant help and support. His advice and patience carried me through all the stages of this thesis work: tips for programming, suggestions for academic writing, countless hours of discussion and sharing ideas and experiences on exchange measurements with me. I would also like to express my profound gratitude to my examiner, Dr. Evren Özarslan, for introducing me to the field of diffusion magnetic resonance, giving me the precious opportunity to work on this project, and his insightful suggestions on my thesis work. Without their guidance, this work would not be possible to be completed.

Many thanks to Anders Eklund for partially funding the MR scanner employed in this thesis work, Padraig D'arcy for the help with the preparation of the yeast phantom, Hady Shahin for acquiring the microscopy image of the yeast cells, and David Abramian for discussing the image analysis method for the cell radius estimation.

I would like to extend my thanks to Prof. Ruiliang Bai from Zhejiang University for inspiring us to carry out the project of exchange measurement using the diffusion magnetic resonance technique.

Thanks should also go to my friends and classmates at IMT for being my companions, putting up with me pouring out my stress, and continuously giving me encouragement and motivation during the period of this thesis project. Special thanks to Sumaya for accompanying me to acquire experimental data until midnight.

Last, my deepest love for my parents, 爸爸和妈妈, for your unrequited and unconditional love and support. There are no words to express my appreciation and gratitude for everything you have done for me since the day you brought me into the world.

Linköping, June 21, 2022
Shan Cai 蔡珊

Contents

List of Figures

List of Tables

1 Introduction

This chapter outlines the motivation, aim, objectives and delimitations of this thesis work.

1.1 Motivation

Water exchange across cell membranes is an important physiological process in living cells [1, 2]. Generally, the rate of the exchange process is related to cell membrane permeability [3]. Changes in cell membrane permeability can indicate tissue damage or disease. For example, the membrane permeability has been reported to be increased in tumor cells [4] and brain disorders such as Parkinson's disease [5]. Thus, measurements of water exchange can provide useful biomarkers for the diseases and disorders associated with altered cell membrane permeability.

Diffusion Magnetic Resonance Imaging (dMRI) is a powerful tool that can be used to non-invasively probe water exchange (or membrane permeability) since it is sensitive to the diffusion motion of water molecules. Multiple dMRI-based frameworks have been proposed to measure water exchange, such as Diffusion Exchange Spectroscopy (DEXSY) presented by Callaghan and Furó [6], Diffusion-Exchange Weighted (DEW) Imaging by Ramadan [7, 8], Filter Exchange Spectroscopy (FEXSY) by Åslund et al. [9], FEXSY's imaging version, Filter Exchange Imaging (FEXI) by Lasič et al. [10], and the curvature method by Cai et al. [11]. The DEXSY dataset is a full space dataset acquired with two independently varying diffusion weightings. The information of multi-site exchange processes can be provided by analyzing this dataset. However, in the DEXSY experiment, the large amount of scans significantly increases the acquisition time, limiting DEXSY's clinical application. The FEXSY/FEXI and curvature methods are based on the DEXSY framework but only use a sub set of the DEXSY data, greatly reducing the acquisition time. The DEW method is also a data reduction approach that requires certain samples of the DEXSY dataset. Unlike DEXSY, which assumes two freely-diffusing fractions, the DEW framework assumes diffusion is restricted within cells. FEXI has been shown to characterize brain tumors [12] and breast tumors [13] in vivo, suggesting its potential in clinical applications. Therefore, it is worthwhile to study data reduction methods and investigate alternative schemes to subsample the DEXSY dataset and estimate water exchange.

1.2 Aim and Objectives

A more general mathematical expression based on the DEXSY model is able to describe water exchange. Furthermore, the FEXSY/FEXI and curvature models can be derived from the general model. Theoretically, the general model can be used to analyze the full space DEXSY dataset and certain samples of the DEXSY dataset, i.e., the reduced datasets used in the FEXSY/FEXI, curvature and DEW models. The aim of this thesis work is to experimentally explore the feasibility of measuring water exchange on a low-field benchtop MR scanner using the general, FEXSY/FEXI, curvature and DEW models, and compare the exchange parameters obtained using the general model with different subsampling schemes and the other three models.

The research aim is divided into the four primary objectives as follows:

1. **Implementing the DEXSY experiment on the benchtop MR scanner to acquire a full space dataset.** The sequence used for the DEXSY experiment requires to be modified from a FEXI sequence previously implemented on the benchtop MR scanner.

2. **Analyzing the acquired data using the four models to estimate exchange parameters.** The general model is used to analyze the full space dataset and each reduced dataset. Moreover, each reduced dataset is analyzed using its corresponding data reduction model. The data reduction models include the FEXSY/FEXI, curvature and DEW frameworks.

3. **Comparing the estimated exchange parameters from the four models.** The exchange parameters obtained using the general model on the full space dataset are assumed as "ground truths" for the results obtained using the general model on each reduced dataset and the FEXSY/FEXI and curvature models. The results of the DEW model provide exchange information of the restricted diffusion.

4. **Proposing an alternative subsampling scheme to estimate water exchange.** The data selected by the new subsampling scheme are analyzed using the general model to obtain exchange parameters. The results are assessed by comparing them to the "ground truths".

1.3 Delimitations

This thesis work is limited to an experimental study. The experiment in this thesis work is designed to be conducted on a benchtop scanner (Pure Devices, Rimpar, Germany) and a yeast phantom. The results obtained using the four models are accessed by comparison but not thoroughly validated. This thesis work is not intended to propose a new framework.

2 Theory

This chapter outlines the principles of magnetic resonance imaging (MRI) and diffusion MRI, water exchange measurement models based on diffusion MRI and physical phantoms for exchange measurements.

2.1 Principles of Magnetic Resonance Imaging

Magnetic resonance imaging (MRI) is an imaging modality that can image the internal structures and physiological processes of the human body. Since its introduction in the 1970s, MRI has been widely used in clinics. Its sensitivity to a broad range of tissues, especially its excellent soft tissue contrast, makes it a powerful imaging tool. Furthermore, unlike computed tomography (CT), the absence of ionizing radiation makes MRI a relatively safe procedure [14].

This section briefly introduces how MR images are generated starting from the origin of the MR signal all the way to spatial encoding.

2.1.1 The Origin of the MR Signal

MRI is based on the interaction between nuclear spins and an external magnetic field B_0. In the absence of an external magnetic field, spins exhibit random orientations, resulting in zero net magnetization. When an external magnetic field is introduced, the interaction of spins with the magnetic field leads to spin precession about the magnetic field direction like a gyroscope behaves in gravitation. The precession of a single spin is illustrated in figure 2.1. The precession frequency of spins is called Larmor frequency, and is given by [14]:

$$\omega_0 = \gamma B_0 \tag{2.1}$$

where γ the gyromagnetic ratio, and B_0 the magnetic field strength. The value of γ varies for different nuclei. For the predominant nucleus in MRI, the hydrogen proton, γ is approximately 2.68×10^8 rad/s/T ($\gamma/2\pi$ = 42.58 MHz/T).

3
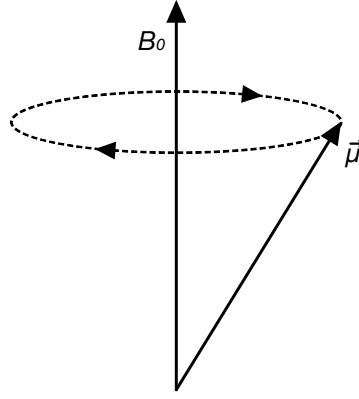
Figure 2.1: Precession of a single spin in an external magnetic field. The magnetic moment $\vec{\mu}$ of a single spin precesses about the external magnetic field B_0.

Spins tend to align to the magnetic field in two possible orientations, parallel or anti-parallel. At thermal equilibrium, the spins parallel to the magnetic field are a few more than the spins anti-parallel to that field. This spin excess results in a net magnetization aligned parallel to the magnetic field. The net magnetization M_0 of a certain sample can be obtained by [14]:

$$M_0 = \frac{\rho_0 \gamma^2 \hbar^2}{4kT} B_0 \tag{2.2}$$

where ρ is the proton density (PD), $\hbar$ the reduced Planck's constant, k the Boltzmann constant, and T the absolute temperature. PD is defined as the number of protons (spins) per unit volume of a certain sample. The net magnetization of a sample can be increased by increasing the strength of the external magnetic field in which the sample is placed. That is why high field MRI is able to generate images with a greater signal-to-noise ratio (SNR) over lower field strengths.

2.1.2 Excitation and Relaxation

In order to obtain a measurable signal from the net magnetization of a sample, a radiofrequency (RF) field B_1 is applied for a brief time. The RF pulse is placed in a plane perpendicular to the direction of the static magnetic field. In the MRI reference frame, the longitudinal axis is defined to be along the direction of the static magnetic field, and thus the RF pulse is on the transverse plane. By tuning the RF pulse to match the Larmor frequency, the net magnetization can be flipped towards the transverse plane. The flip angle α can be controlled by the RF pulse, and is defined by [14]:

$$\alpha = \int_0^t \gamma B_1(\tau) d\tau \tag{2.3}$$

where B_1 is the amplitude of the RF pulse and t is its duration.

The net magnetization continues its precession about the direction of the static magnetic field while being flipped. In order to better illustrate how the RF pulse flips the magnetization, a rotating reference frame is often used, as shown in figure 2.2. The process of flipping the magnetization toward the transverse plane to be detected is referred to as the excitation. The transverse component of the precessing magnetization can be detected by a receiver RF coil via induction. The induced voltage is the actual MR signal, which is referred to as the free induction decay (FID) signal [14].
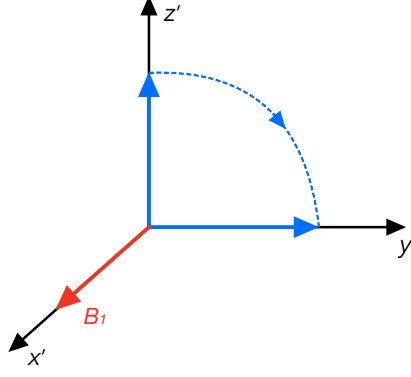
Figure 2.2: The effect of an RF pulse on the magnetization in a rotating reference frame. The transverse plane (x'-y') of this reference frame rotates about the longitudinal direction at the Larmor frequency. When an RF pulse (red) is applied along x', the magnetization (blue) rotates around x' with a flip angle given by the RF pulse. The flip angle is illustrated as $90°$ in this figure, and a $90°$ RF pulse is commonly referred to as an excitation RF pulse.

Once the RF pulse is turned off, the magnetization will start to return to its initial state. This process is referred to as relaxation. There are two types of relaxation: longitudinal relaxation and transverse relaxation. The longitudinal magnetization M_z tends to recover its original magnitude as shown in figure 2.3. The regrowth of M_z can be described by [14]:

$$M_z(t) = M_z(0)e^{-t/T_1} + M_0(1 - e^{-t/T_1}) \tag{2.4}$$

where M_0 is the longitudinal magnetization at equilibrium and $M_z(0)$ is the longitudinal magnetization immediately after applying an RF pulse. T_1 is the time when the longitudinal magnetization recovers 63% of M_0 as illustrated in figure 2.3.
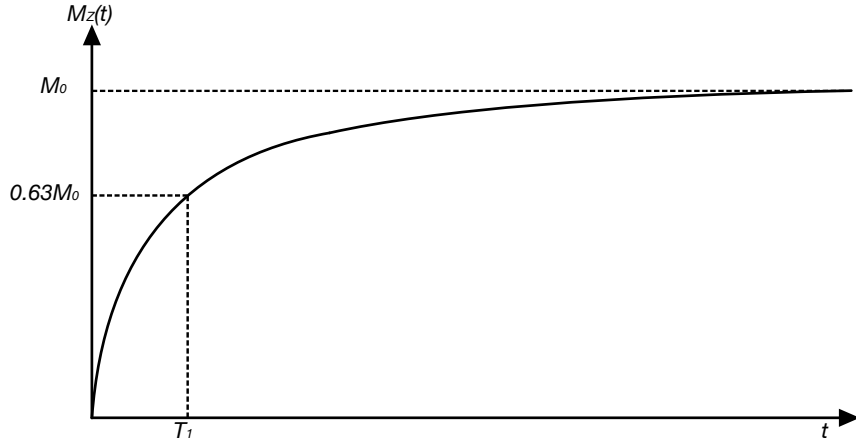
Figure 2.3: Longitudinal relaxation. In this case, the initial condition of the longitudinal magnetization is $M_z(0) = 0$.

The newly produced transverse magnetization M_{xy} will start to decay due to the dephasing of spins. The variations in the local magnetic fields experienced by spins cause a difference in their precessional frequency. The incoherence of precessional frequencies results in phase dispersion and consequently leads to the attenuation of the transverse magnetization. This decay can be characterized by a time constant T_2 as illustrated in figure 2.4, and is given by [14]:

$$M_{xy}(t) = M_{xy}(0)e^{-t/T_2} \tag{2.5}$$

where $M_{xy}(0)$ is the transverse magnetization immediately after applying an RF pulse. In practice, the presence of inhomogeneities of the magnetic field accelerates the transverse relaxation process. The time constant used to characterize this decay is T_2^* [14]. The total attenuation in magnetization can be described by replacing T_2 in equation 2.5 with the newly introduced T_2^*. Similarly, T_2^* can characterize the decay rate of the previously mentioned FID signal. It is important to note that the relaxation due to the macroscopic magnetic field inhomogeneities is reversible, but the T_2 relaxation caused by the variation in the local magnetic fields is not [14].
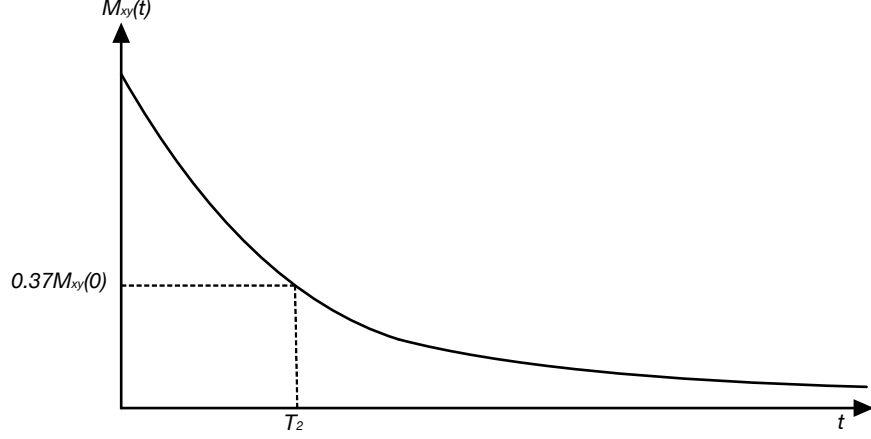
Figure 2.4: Transverse relaxation. T_2 is the time when the transverse magnetization has reduced to 37% of its original magnitude.

A spin-echo is generally used in MRI and can be generated by applying a second RF pulse with a flip angle of 180°, referred to as a refocusing pulse, at a certain time after the application of a 90° RF pulse. The refocusing pulse reverses the accumulated phase of the spins and consequently results in a spin-echo. This process will additionally reverse the dephasing due to the magnetic field inhomogeneities, resulting only in a T_2-dependent decay in the generated echo. The spin-echo imaging sequence diagram is presented at the end of this section after introducing spatial encoding.

2.1.3   Spatial Encoding

The third indispensable magnetic field in MRI is the gradient field, which makes it possible to localize the measured MR signal. The gradient field usually consists of three orthogonal gradient systems that generate spatially dependent magnetic fields superimposed on the main magnetic field. When spins are placed in a spatially changing magnetic field, their precessional frequencies are spatially varying as well. For example, with a general gradient vector $\mathbf{G}$, which generates a magnetic field varying linearly along with a general direction $\mathbf{r}$, the precession frequency in equation 2.1 can be rewritten as [14]:

$$\omega(\mathbf{r}) = \gamma \left(B_0 + \mathbf{r} \cdot \mathbf{G} \right) \tag{2.6}$$

Three procedures are usually applied with the gradient fields to locate a signal spatially. They are: slice selection, frequency encoding, and phase encoding. To better describe these techniques, in the case of acquiring a 2D image, assume slice selection is applied along the z-axis, frequency encoding along the x-axis, and phase encoding along the y-axis. Note that, in practice, they can be applied along any axis or a combination of axes to manipulate the orientation of a selected slice.

Slice Selection

The slice selection gradient is applied during the application of the RF pulse to only excite a specific slice with a certain thickness. Recalling the spatially varying precession frequency in equation 2.6, only the slice with the precession frequency matching the frequency of the RF pulse can be excited. Thus, the position of the slice can be changed by varying the center frequency of the RF pulse. The slice thickness Δz can be derived from equation 2.6 and is given by equation 2.7. The slice thickness can be adjusted by changing the bandwidth of the RF pulse $\Delta \omega$.

$$\Delta z = \frac{\Delta \omega}{\gamma G_z} \tag{2.7}$$

Frequency and Phase Encoding

After the slice has been excited, the next step is to locate the in-plane MR signal. Frequency and phase encoding are applied for this purpose. The spatially encoded signal is stored in a data matrix, which is referred to as *k-space*, as illustrated in figure 2.5. K-space contains the spatial frequency information of an image and is defined by [14]:

$$k(t) = \frac{\gamma}{2\pi} \int_0^t G(\tau) \mathrm{d}\tau \tag{2.8}$$
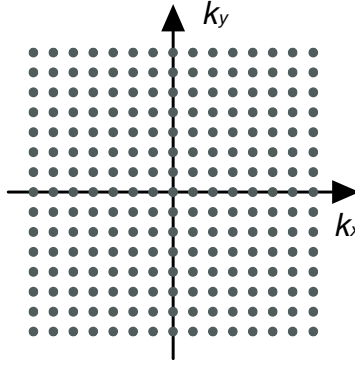
Figure 2.5: K-space data matrix. Each data point in k-space corresponds to a particular combination of frequency and phase encoding.

Frequency encoding introduces a frequency difference in the detected signal along the frequency encoding direction [14]. This is obtained via the application of a gradient during the readout of the signal, corresponding to a line of data in the k-space.

Phase encoding induces a space-dependent phase difference between spins along the phase encoding direction by applying gradients before the readout. The gradients are in different amplitudes but with same duration for each repetition of a sequence. During phase encoding, the precessional frequencies of spins are varied, resulting in the dephasing of spins. After the phase encoding gradient is turned off, the spins return to process with the same frequency but keep their different phases [14]. The signal with phase variation is then detected with frequency encoding and stored in k-space as a line of data as mentioned before. To fill the k-space, multiple repetitions of the sequence with different phase encoding gradients are required. The varying phase encoding gradients correspond to a line-to-line movement in the k-space.

The signal stored in k-space, $s(k_x, k_y)$, can be described by [14]:

$$s(k_x, k_y) = \iint \rho(x, y) e^{-i2\pi(xk_x + yk_y)} dx dy \tag{2.9}$$

7

where $\rho(x,y)$ is the spin density of a voxel in the selected slice located at position (x,y). The spin density image can be reconstructed by performing an inverse 2D Fourier transform of k-space data:

$$\rho(x,y) = \iint s(k_x, k_y) e^{i2\pi(xk_x + yk_y)} dk_x dk_y \tag{2.10}$$

2.1.4 Spin-Echo Imaging Sequence

The spin-echo imaging sequence is one of the most commonly used sequences in MRI. The sequence employed in this thesis work is also based on the spin-echo sequence. As shown in figure 2.6, the spin-echo imaging sequence includes a 90° excitation RF pulse, followed by a 180° refocusing RF pulse, and three gradients used for slice selection, phase encoding and frequency encoding. Repetition time (TR) and echo time (TE) are the two time parameters in this sequence. TR is the time between successive pulse sequences in the same slice. TE represents the time from the 90° pulse to the refocused echo, which is twice as long as the time between the 90° and 180° RF pulses.
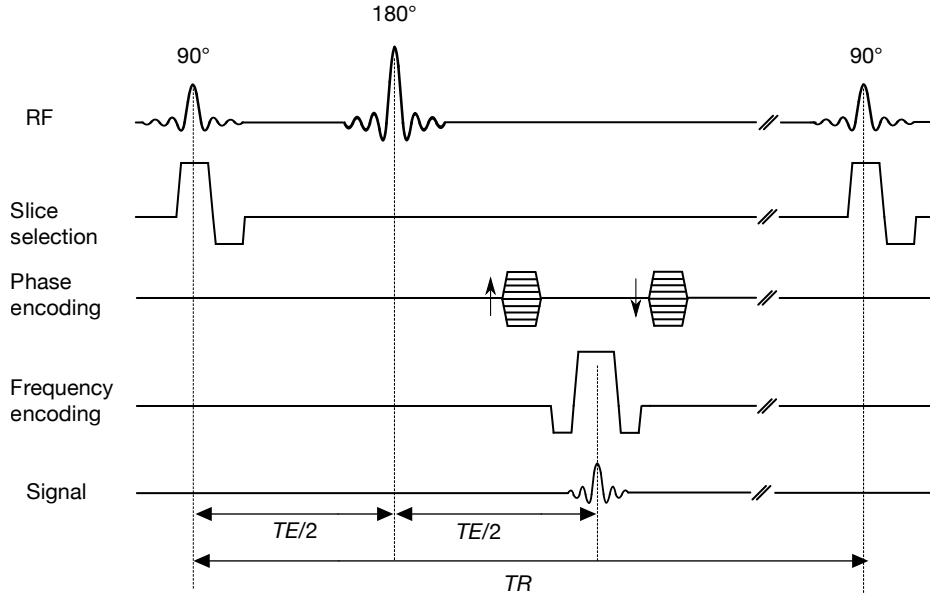
Figure 2.6: Spin-echo imaging pulse sequence diagram. An echo is produced by a pair of 90° excitation and 180° refocusing RF pulses. Slice selection is applied during the application of the 90° pulse. Phase encoding is later turned on before the echo acquisition. Stepped gradient pulses of the phase encoding illustrate that the gradient strength varies for each repetition. Arrows indicate their varying directions. Finally, frequency encoding is applied during the echo readout. The downward gradient pulses in the slice selection and frequency encoding and the additional phase encoding gradients located after the echo are designed to compensate for all gradient dephasing between successive repetitions.

The time parameters of the spin-echo sequence can be adjusted to generate images with different contrast mechanisms, such as T_1-, T_2-, and PD-weighted images [14]. Different tissues with different properties can be distinguished in an MR image by applying these contrast mechanisms. The time parameters and effects of the three contrast mechanisms are summarized as follows:

- T_1-weighted: short TR and TE; tissues with short T_1 display high intensity;

8

- T_2-weighted: long TR and TE; tissues with long T_2 display high intensity;

- PD-weighted: long TR and short TE; tissues with high PD display high intensity.

Another mechanism based on diffusional motion of water molecules to generate contrast is referred to as Diffusion Magnetic Resonance Imaging (dMRI), which will be introduced in the next section.

2.2 Principles of Diffusion Magnetic Resonance Imaging

Diffusion is often described as a transport process of molecules and particles moving down their concentration gradients, resulting in mixing or mass transport. This movement does not require bulk motion. Fick's first law explains the diffusion phenomenon by relating the diffusive flux of particles to the concentration gradient through the following equation [15]:

$$\mathbf{J} = -D\nabla C \tag{2.11}$$

where $\mathbf{J}$ is the net flux vector of particles, ∇C the concentration gradient, and D the diffusion coefficient. Fick's first law indicates there is no net flux in the absence of a concentration gradient. However, diffusion can also occur in thermodynamic equilibrium without temperature or concentration gradients. The movement of particles under these conditions was first observed by Robert Brown [16], and is referred to as Brownian motion. Albert Einstein [17, 18] further introduced a probabilistic framework to determine the displacement of an ensemble of particles resulting from the Brownian random motion within a certain time. The mean-squared displacement of the freely diffusing particles increases linearly as the diffusion time:

$$\langle x^2 \rangle = 2nD\Delta \tag{2.12}$$

where $\langle x^2 \rangle$ is the mean-squared displacement of an ensemble of particles, D is its diffusing coefficient, n stands for a constant number of dimensionality and Δ represents the diffusion time. Einstein linked the concepts of the Brownian motion to diffusion coefficient of Fick's laws.

Magnetic resonance can serve as a probe of molecular diffusion. It was first proposed by Erwin Hahn [19] in 1950, when he recognized that molecular diffusion could cause the dephasing of spins. Later, in 1954, Carr and Purcell [20] proposed a direct measurement of molecular diffusion using a constant field gradient in the spin-echo experiment. After about ten years, Stejskal and Tanner [21] developed a pulsed gradient spin-echo (PGSE) sequence to measure diffusion, which is the predominant diffusion measurement still in use today. The PGSE sequence is illustrated in figure 2.7. This scheme simplified the mathematical analysis by introducing narrow gradient pulses, for which it can be assumed that diffusion does not occur during their application ($\delta \ll \Delta$). This is referred to as the short gradient pulse (SGP) approximation.

As shown in figure 2.7, the 180° RF pulse applied between the two gradient pulses makes it possible for the second gradient pulse to reverse the phase change of spins induced by the first gradient pulse [15]. For static spins, the net dephase introduced by the two gradient pulses is zero; however, for moving spins, the dephasing due to the first pulse cannot be completely canceled by the second one. The net dephasing of a moving spin is proportional to its displacement along the direction of the diffusion gradient, and is given by [15]:

$$\phi_2 - \phi_1 = -q\left(x_2 - x_1\right) \tag{2.13}$$

where ϕ and x represent the phase accumulation and the position of a spin after the application of a gradient pulse, respectively. The subscripts 1 and 2 refer to the time points when
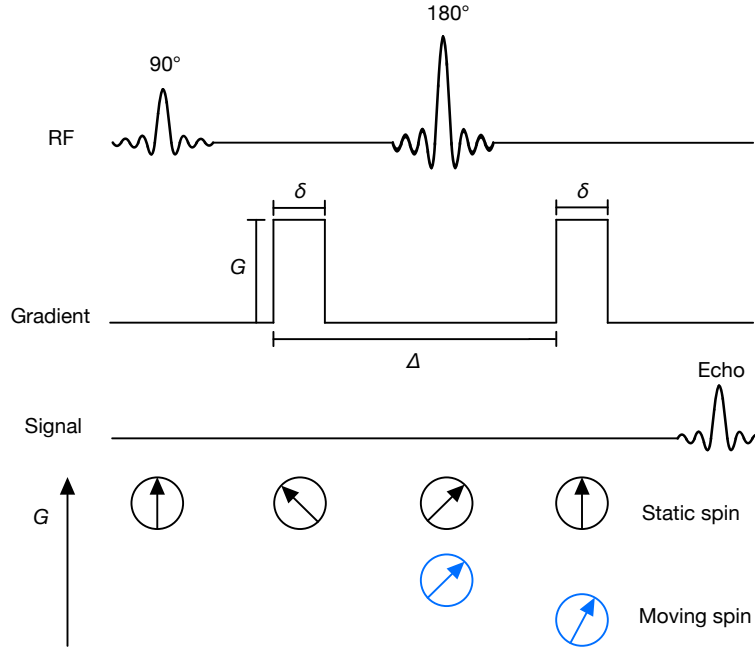
Figure 2.7: Stejskal and Tanner pulsed gradient spin-echo (PGSE) sequence. An echo is produced by a pair of 90° excitation and 180° refocusing RF pulses. Two gradient pulses with amplitude G are separated by the 180° RF pulse. The gradient pulse duration is denoted as δ, and the time between the application of the two gradient pulses is denoted as Δ, referred to as *diffusion time*. The gradient pulses can be applied in any direction. The arrow inside circles represents the phase of a spin.

the first and the second gradient pulses were applied, respectively. In this expression, q is a quantity that describes the applied gradient waveform. For a rectangular gradient pulse as shown in figure 2.7, $q = \gamma \delta G$. The quantity q can also be defined for a general gradient waveform through the following expression [22]:

$$q = \gamma \int_0^t G(\tau)d\tau \tag{2.14}$$

The net dephasing of moving spins leads to phase dispersion and, consequently, attenuation of the MR signal. A new quantity, $E(q)$, is introduced to describe the signal attenuation caused by diffusion. In order to eliminate the effect of relaxation-related signal attenuation, $E(q)$ is obtained by normalizing the diffusion-attenuated signal $S(q)$ with a measurement obtained without applying diffusion gradients S_0. Accordingly, $E(q) = S(q)/S_0$, is solely dependent on diffusion.

Under the assumption of free diffusion, where the displacement distribution is Gaussian, the MR signal attenuation, $E(q)$, can be described by another Gaussian, and is given by [15]:

$$E(q) = e^{-q^2 D(\Delta - \frac{\delta}{3})} \tag{2.15}$$

Equation 2.15 is obtained by taking the pulse duration δ into consideration in the Stejskal and Tanner's original experiment. In clinical applications, a quantity, *b-value* or b, is commonly

used to describe the degree of diffusion weighting, which is defined by [15]:

$$b = q^2(\Delta - \frac{\delta}{3})$$
$$= \gamma^2\delta^2 G^2(\Delta - \frac{\delta}{3}) \tag{2.16}$$

The signal attenuation in equation 2.15 can then be rewritten as a function of b:

$$E(b) = e^{-bD} \tag{2.17}$$

As mentioned before, the expressions of q, and consequently b, depend on the shape of the applied gradient waveform. Equation 2.16 is formulated assuming that ideal rectangular gradient pulses are applied. However, MR scanners cannot generate perfect rectangular gradient pulses in practice. Instead, a rise time (or ramp-up time) is required for the MR scanner to reach a certain gradient strength, and consequently, symmetric trapezoidal pulses are produced, as visualized in figure 2.8. By introducing the rise time ε, b can be expressed by [23]:

$$b = \gamma^2 G^2 \left[\delta^2 \left(\Delta - \frac{\delta}{3} \right) + \frac{\varepsilon^3}{30} - \frac{\delta\varepsilon^2}{6} \right] \tag{2.18}$$
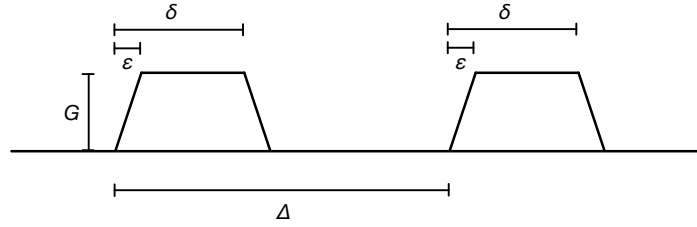
Figure 2.8: Trapezoidal diffusion gradient pulses.

Diffusion is expected to be Gaussian if diffusion is free as previously introduced. The diffusion coefficient D based on the assumption of Gaussian diffusion is an intrinsic characteristic of the medium itself. However, diffusion is restricted in complex media and thus deviates from the Gaussian approximation. The *Apparent Diffusion Coefficient (ADC)* is then introduced as a global and statistical parameter to indirectly measure the *intrinsic diffusion coefficient (D)*, and will depend on experimental parameters, such as the voxel size and *b-values* [24]. Essentially, the *ADC* represents a contribution average of all the water molecules within the measured voxel [25]. Rewriting equation 2.17 using the *ADC* instead of *D*, gives:

$$E(b) = e^{-bADC}$$
$$S(b) = S_0 e^{-bADC} \tag{2.19}$$

Equation 2.19 serves as a mathematical model for estimating the *ADC*. At least two measurements with different *b-values* are required to calculate the unknown values of *ADC* and S_0 [24].

Diffusion Tensor Imaging (DTI) is a scheme employed to characterize diffusion in terms of anisotropy, proposed by Basser et al. in 1994 [26] . For anisotropic media, such as white matter [27], diffusion occurs mostly along the nerve fibers. In this case, a scalar *ADC* is inadequate to describe the orientation-dependent diffusion [15]. DTI serves as an essential tool to characterize anisotropic diffusion through the diffusion tensor, **D**, which is a symmetric matrix representing diffusion along different directions [24, 21]:

$$\mathbf{D} = \begin{bmatrix} D_{xx} & D_{xy} & D_{xz} \\ D_{xy} & D_{yy} & D_{yz} \\ D_{xz} & D_{yz} & D_{zz} \end{bmatrix} \tag{2.20}$$

Equation 2.19 can be rewritten in terms of the diffusion tensor as follows:

$$S(b, \hat{g}) = S_0 e^{-b\hat{g}^T \mathbf{D} \hat{g}} \tag{2.21}$$

where $\hat{g}$ is a unit vector of the diffusion gradient direction.

Mean diffusivity (MD) and *fractional anisotropy (FA)* are two commonly used scalar metrics obtained from DTI. *MD* and *FA* can be obtained from the eigenvalues (λ_1, λ_2 and λ_3) of the diffusion tensor using equations 2.22 and 2.23, respectively [28].

$$MD = \frac{\lambda_1 + \lambda_2 + \lambda_3}{3} \tag{2.22}$$

$$FA = \sqrt{\frac{1}{2}} \frac{\sqrt{(\lambda_1 - \lambda_2)^2 + (\lambda_2 - \lambda_3)^2 + (\lambda_3 - \lambda_1)^2}}{\sqrt{\lambda_1^2 + \lambda_2^2 + \lambda_3^2}} \tag{2.23}$$

MD is the average of the eigenvalues and represents the mean diffusivity of all diffusion directions. *FA* is the normalized variance of the eigenvalues and ranges from 0 to 1. For an *FA* value which tends to 0, diffusion tends to be completely isotropic; while for an *FA* value which tends to 1, diffusion is completely anisotropic.

2.3 Diffusion-Based Water Exchange Measurement

Water exchange measurement is one of the clinical applications of dMRI. Over the years, multiple diffusion-based MR methods have been proposed to measure water exchange. This section briefly reviews the development of diffusion-based exchange measurements and primarily introduces the theories behind the four methods implemented in this thesis work. The four methods are: a general model based on Diffusion Exchange Spectroscopy (DEXSY) which was proposed in 2004 [6], Diffusion-Exchange Weighted (DEW) Imaging in 2006 [7, 8], Filter Exchange Spectroscopy/ Imaging (FEXSY/FEXI) presented in 2009/2011 [9, 10] and the curvature method in 2018 [11].

2.3.1 Review on Water Exchange Models

In a cellular environment, water exchange is a process through which water molecules move across a cell membrane in both directions. There are two parameters used to characterize the exchange process, the *exchange rate*, *k*, and its inverse, the *mean residence time* or *mean life time*, τ. The first parameter describes how fast the molecules exchange between spaces, and the latter the average time a molecule spends inside a certain space before leaving.

Water exchange rate has been often suggested to describe membrane permeability, but the direct relationship between those two parameters is not clear. In 1983, Brahm [3] proposed an equation to generally relate the membrane permeability to the exchange rate. The relationship is presented in equation 2.24, in which the membrane permeability *P* is proportional to the exchange rate from intra- to extracellular space (k_{ie}) and the cell volume-to-surface ratio (V/A). For spherical cells, the expression can be simplified using the cell radius *r* as presented in equation 2.25 [9, 29].

$$P = k_{ie} \frac{V}{A} \tag{2.24}$$

$$P = k_{ie} \frac{r}{3} \tag{2.25}$$

A two-compartment system is frequently employed to describe water exchange, in which the intra- and extracellular compartments present different diffusion coefficients, and the exchange rate during the process is considered to be a constant.

12

In 1985, Kärger [30] introduced an analytical model to study the diffusion-weighted signal obtained from a PGSE experiment, accounting for water exchange between two compartments. Water exchange is probed by introducing the dependence of the mean residence time to each compartment's diffusion coefficient. The Kärger model assumes that diffusion in both compartments is free, and it was later developed by Price et al. [31] to include restricted diffusion in one compartment (i.e., the intracellular site). Based on the previous work by Kärger and Price et al., in 2009, Ramadan [8] proposed a new analysis framework, which is named diffusion-exchange-weighted (DEW) imaging, to estimate the mean residence time of each compartment. The DEW sequence consists of two identical PGSE blocks separated by an exchange time, during which molecules exchange between the two compartments. Ramadan's experiment observes an increase in the estimated *ADC* value at longer exchange times, which can be explained by the strengthened exchange effect caused by the long exchange time.

In 2004, Callaghan and Furó [6] proposed the Diffusion Exchange Spectroscopy (DEXSY) technique to characterize exchange using a two-dimensional (2D) diffusion encoding PGSE measurement. The acquisition sequence used in DEXSY is also composed of two PGSE blocks separated by a varying mixing time. The two PGSE blocks in DEXSY are encoded with two independently varied *b-values*, resulting in a 2D dataset being acquired. The 2D dataset is analyzed using a 2D inverse Laplace transform (ILT) [32], producing a 2D diffusivity map. Off-diagonal peaks in the 2D map represent the molecules that have exchanged between compartments during the mixing time. The DEXSY measurement needs to be performed with multiple mixing times to quantify the exchange process. Thus, this 3D acquisition looping through the two *b-values* and the mixing time significantly increases the scan time, limiting the clinical application of a full DEXSY acquisition.

In 2009, Åslund et al. [9] proposed a data reduction method based on the DEXSY experiment, named Filter Exchange Spectroscopy (FEXSY). In the FEXSY framework, the first PGSE block serves as a filter with a constant and large *b-value* employed to completely attenuate the signal of fast diffusing water molecules in the extracellular compartment. During the mixing time, water molecules are assumed to exchange from one compartment to another. The remaining signal affected by exchange is then encoded by the second PGSE block, referred to as the detection block, with a series of *b-values*. The FEXSY strategy makes it possible to slice a DEXSY dataset to characterize water exchange, thus significantly reducing the acquisition time. The imaging version of FEXSY was later presented by Lasič et al. [10], referred to as Filter Exchange Imaging (FEXI), which introduces the *apparent exchange rate* (AXR) as an estimate to the effective exchange rate (k). FEXI has been shown to be feasible to map the AXR in human brain in vivo and differentiate healthy and brain tumor tissue [12].

After about a decade, Cai et al. [11] introduced a curvature scheme to reduce the acquisition time in the DEXSY experiment. This approach slices the 2D DEXSY dataset along an anti-diagonal (in which the sum of the two *b-values* is constant) and only requires as few as four data points for each mixing time. The exchange rates can then be estimated by repeating the measurement with several mixing times.

The FEXSY/FEXI and curvature methods are data reduction approaches based on the DEXSY framework, which assumes free diffusion in both compartments. On the other hand, the DEW method is a data reduction method considering that diffusion is restricted in the intracellular compartment. The acquisition sequences used in these four methods are based on a double diffusion encoding (DDE) sequence. As an example, figure 2.9 shows the double diffusion encoding sequence used for DEXSY. The full (b_1, b_2) sampling space acquired in DEXSY contains the data used in the FEXSY/FEXI, curvature and DEW experiments. The acquisition trajectories employed in these methods are illustrated in figure 2.10.
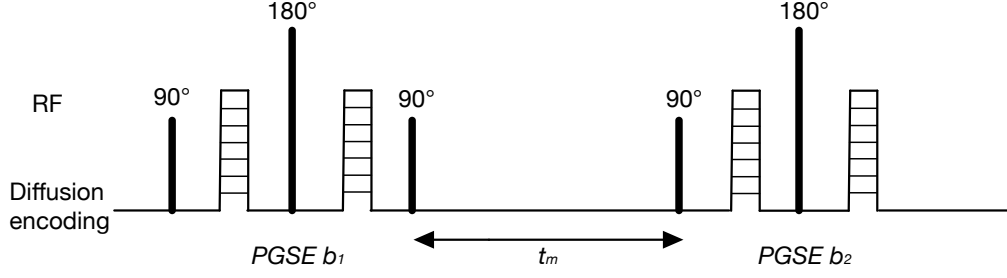
Figure 2.9: Double diffusion encoding sequence used for DEXSY. The sequence consists of two PGSE blocks with b_1 and b_2 varied independently (illustrated as stepped gradient pules). A varying mixing time t_m separates the two PGSE blocks. The second 90° RF pulse rotates the refocused transverse magnetization to the longitudinal axis, where the magnetization weighted by the first diffusion encoding block is stored during the mixing time. The third 90° RF pulse flips the stored longitudinal magnetization to the transverse plane, where the second diffusion encoding is applied. By applying the second pair of 90°-180° RF pulses, a stimulated echo (STE) is produced, which is weighted by the two diffusion encoding blocks and water exchange.

(a) FEXSY/FEXI trajectory.   (b) Curvature trajectory.   (c) DEW trajectory.
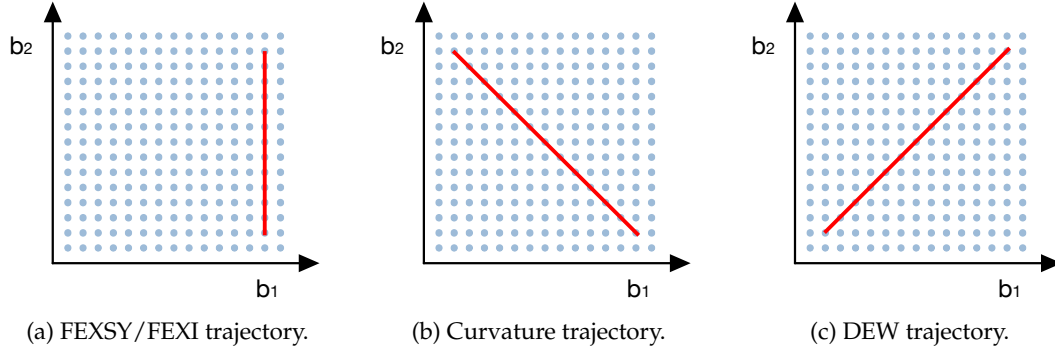
Figure 2.10: Data acquisition trajectories of the four methods (for a single mixing time). The 2D DEXSY data are illustrated as blue dots, showing a data matrix with all varied b_1 and b_2 within the set range. The three data reduction methods only use certain samples of the 2D DEXSY dataset. The acquisition trajectory colored in red is shown as one trajectory example of each data reduction method. (a) In the FEXSY/FEXI experiment, b_1 is constant (a large value is chosen to filter the fast diffusion contribution), and b_2 is varied. (b) In the curvature experiment: the sum of b_1 and b_2 is constant. (c) In the DEW experiment: $b_1 = b_2$.

2.3.2 General Model

For a two-compartment exchange system with compartments a and b as illustrated in figure 2.11, the DDE signal attenuation in the DEXSY experiment can be expressed as weighted contributions of all sub-ensembles [11]:

$$E(b_1, b_2) = f_{aa}e^{-b_1 D_a - b_2 D_a} + f_{ab}e^{-b_1 D_a - b_2 D_b} + f_{bb}e^{-b_1 D_b - b_2 D_b} + f_{ba}e^{-b_1 D_b - b_2 D_a} \qquad (2.26)$$

where D_a and D_b are the intrinsic diffusion coefficients of compartments a and b, respectively. f with different subscripts denotes the fractional population of the corresponding sub-ensemble: f_{aa} represents the population residing in compartment a during both diffusion encodings, f_{ab} represents the population in compartment a during the first diffusion

14
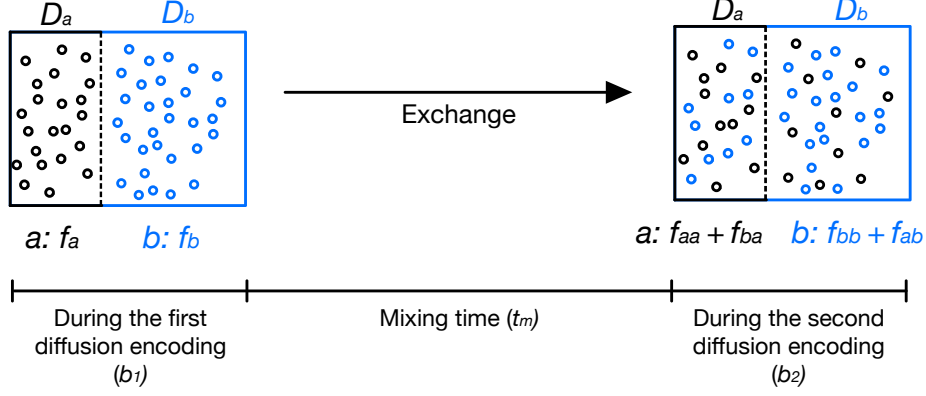
Figure 2.11: A two-compartment water exchange system. Particles originally in compartment a are shown as black circles, and in compartment b as blue circles. Molecule motion is probed by double diffusion encodings separated by a mixing time t_m. At equilibrium, the fractional populations of two compartments are denoted as f_a and f_b, respectively. f_{aa} and f_{bb} are non-exchanging fractions, and f_{ab} and f_{ba} are exchanging fractions during t_m.

encoding and in compartment b during the second diffusion encoding, and similarly for the other two.

Subjected to mass conservation, the fractional populations are related by the following conditions:

$$f_a = f_{aa} + f_{ab} \tag{2.27}$$
$$f_b = f_{bb} + f_{ba} \tag{2.28}$$
$$f_a + f_b = 1 \tag{2.29}$$
$$f_{aa} + f_{ab} + f_{bb} + f_{ba} = 1 \tag{2.30}$$

It is important to note that equation 2.26 is based on certain assumptions which are also used in the FEXSY/FEXI and the curvature models. The assumptions are presented as follows:

- Diffusion in both compartments is free (Gaussian);

- Exchange occurs only during the mixing time and not during diffusion encoding blocks;

- The relaxation times (T_1 and T_2) are the same, or very similar, for both compartments.

For steady-state exchange, the exchanging fractional populations are related by the condition as follows [11]:

$$f_{ab} = f_{ba} = \frac{f}{2} \tag{2.31}$$

where f_{ab} is the exchanging fractional population from compartment a to compartment b, f_{ba} the exchanging fractional population in the reverse direction, and f the total exchanging fractional population. f_{ab} and f_{ba} can be modeled as functions of the mixing time according to first-order exchange kinetics [33]:

$$f_{ab}(t_m) = \frac{f_a k_{ab}}{k_{ab} + k_{ba}} \left(1 - e^{-(k_{ab} + k_{ba})t_m} \right) \tag{2.32}$$

$$f_{ba}(t_m) = \frac{f_b k_{ba}}{k_{ab} + k_{ba}} \left(1 - e^{-(k_{ab} + k_{ba})t_m} \right) \tag{2.33}$$

where k_{ab} and k_{ba} are the forward and backward exchange rates between compartments a and b. They comprise the effective exchange rate k, which is given by equation 2.34. Note that equations 2.32 and 2.33 are formulated with the initial conditions $f_{ab}(0) = 0$ and $f_{ba}(0) = 0$.

$$k = k_{ab} + k_{ba} \tag{2.34}$$

According to the principle of microscopic reversibility [34], the average forward and backward reaction rates for exchange in equilibrium are equal:

$$f_a k_{ab} = f_b k_{ba} \tag{2.35}$$

Using the conditions in equations 2.35 and 2.29, the fractional population of each compartment can be rewritten as:

$$
\begin{aligned}
f_a &= \frac{k_{ba}}{k_{ab} + k_{ba}} \\
f_b &= \frac{k_{ab}}{k_{ab} + k_{ba}}
\end{aligned}
\tag{2.36}
$$

Incorporating equations 2.36 and 2.29 to equations 2.32 and 2.33, yields:

$$f_{ab}(t_m) = f_{ba}(t_m) = f_a(1 - f_a)(1 - e^{-kt_m}) \tag{2.37}$$

By introducing the dependency of the mixing time t_m from $f_{ab}(t_m)$ and $f_{ba}(t_m)$ in equation 2.37 to the signal attenuation and using conditions between the fractions (equations 2.27, 2.28 and 2.29), equation 2.26 can be rearranged as follows:

$$
\begin{aligned}
E(b_1, b_2, t_m) =\; & e^{-b_2 D_a} \left[f_a e^{-b_1 D_a} + f_a(1 - f_a)(e^{-b_1 D_b} - e^{-b_1 D_a})(1 - e^{-kt_m}) \right] + \\
& e^{-b_2 D_b} \left[(1 - f_a)e^{-b_1 D_b} + f_a(1 - f_a)(e^{-b_1 D_a} - e^{-b_1 D_b})(1 - e^{-kt_m}) \right]
\end{aligned}
\tag{2.38}
$$

Equation 2.38 is referred to as the general model for estimating water exchange used in this thesis work.

2.3.3 FEXSY/FEXI Model

FEXSY assumes a two-compartment system with significantly different diffusion coefficients in a cellular setting. The diffusion coefficient in the intracellular compartment is considered lower than in the extracellular compartment. For unifying the notations used throughout this thesis work, compartment a is denoted as the intracellular compartment and b the extracellular one. For a single PGSE experiment in the absence of water exchange, the signal attenuation is given by [9]:

$$S(b) = S_0(f_a e^{-bD_a} + f_b e^{-bD_b}) \tag{2.39}$$

The equilibrium fractional populations f_a and f_b fulfill the condition in equation 2.29.

In the FEXSY experiment, the filter block (the first PGSE block) is applied to suppress the contribution from the population in the extracellular compartment. Subsequently, molecules exchange between compartments during the mixing time, resulting in a change in the fractional population of each compartment. The fractional population of the extracellular compartment during t_m is given by [9] :

$$f_b(t_m) = f_b - (f_b - f_b(0))e^{-kt_m} \tag{2.40}$$

where $f_b(0)$ is the initial fractional population of the extracellular compartment during the exchange process. Equation 2.40 obeys the first order reaction kinetics [35]. In FEXSY, equations 2.39 and 2.40 are used to fit experimental data and estimate k [9].

In the FEXI experiment, t_m is introduced to the signal attenuation model $S(b, t_m)$ [10]:

$$S(b, t_m) = S_f(t_m)(f_a(t_m)e^{-bD_a} + f_b(t_m)e^{-bD_b}) \qquad (2.41)$$

where $S_f(t_m)$ stands for the signal intensity before applying the detection block (the second PGSE block). The attenuation due to T_1 relaxation during t_m is included in $S_f(t_m)$. For low *b-values*, by using Taylor series expansion and condition 2.29, the signal attenuation in equation 2.41 can be approximated to [10]:

$$S(b, t_m) = S_f(t_m)e^{-ADC'(t_m)b} \qquad (2.42)$$

where ADC' is defined by the weighted average of the contributions from both compartments as presented in equation 2.43. Similarly, the ADC at equilibrium, ADC_{eq}, is given by equation 2.44.

$$ADC'(t_m) = f_a(t_m)D_a + f_b(t_m)D_b \qquad (2.43)$$
$$ADC_{eq} = f_aD_a + f_bD_b \qquad (2.44)$$

Inserting equations 2.40, 2.29 and 2.44 into equation 2.43, yields the expression [10]:

$$ADC'(t_m) = ADC_{eq}(1 - \sigma e^{-t_m AXR}) \qquad (2.45)$$

where

$$\sigma = 1 - \frac{ADC'(0)}{ADC_{eq}} \qquad (2.46)$$

is the *filter efficiency*, which quantifies the reduction percentage of ADC_{eq} after the application of the filter block. *Apparent Exchange Rate (AXR)* is an estimate to the efficient exchange rate (k) as mentioned before. With large AXR, ADC' will return back to its equilibrium value faster. Similar to the concept of *Apparent Diffusion Coefficient* (ADC) presented in section 2.2, AXR is also dependent on the assumptions and parameters set in the experiment.

Equations 2.42 and 2.45 are used in the FEXI experiment to estimate AXR, ADC_{eq} and σ. In this thesis work, the FEXI method is used to estimate water exchange.

2.3.4 Curvature Model

The curvature method assumes the water exchange process between the two compartments is at steady-state. In this framework, the parameters b_1 and b_2 are rearranged to b_s and b_d according to equation 2.47 [11]. The parameter b_s is kept constant and the value range of b_d is set to $[-b_s, b_s]$.

$$\begin{aligned} b_s &= b_1 + b_2 \\ b_d &= b_2 - b_1 \end{aligned} \qquad (2.47)$$

By using b_s and b_d, equation 2.26 can be rewritten as [11]:

$$E(b_s, b_d) = f_{aa}e^{-b_sD_a} + f_{bb}e^{-b_sD_b} + e^{-b_sD_s}(f_{ab}e^{-b_dD_d} + f_{ba}e^{b_dD_d}) \qquad (2.48)$$

where

$$\begin{aligned} D_s &= \frac{(D_a + D_b)}{2} \\ D_d &= \frac{(D_b - D_a)}{2} \end{aligned} \qquad (2.49)$$

Recalling equation 2.31 for steady-state exchange, equation 2.48 can be rearranged as:

$$E(b_s, b_d) = f_{aa}e^{-b_sD_a} + f_{bb}e^{-b_sD_b} + fe^{-b_sD_s}\cosh(b_dD_d) \qquad (2.50)$$

Taking the second derivative of E in equation 2.50 with respect to b_d, yields:

$$\frac{\partial^2 E}{\partial b_d^2} = f D_d^2 e^{-b_s D_s} \cosh(b_d D_d) \tag{2.51}$$

Equations 2.50 and 2.51 indicate that, for steady-state exchange, the signal intensity as a function of b_d (at constant b_s) is a hyperbolic curve, which is symmetric about $b_d = 0$ and has positive curvature since $f > 0$. The curvature of the signal is proportional to the exchanging fractional population f. Assuming $D_d \neq 0$ ($D_a \neq D_b$), by evaluating equation 2.51 at $b_d = b$, f can be expressed by:

$$f = \left(\left. \frac{\partial^2 E}{\partial b_d^2} \right|_{b_d=b} \right) \frac{e^{b_s D_s}}{\cosh(b_d D_d) D_d^2} \tag{2.52}$$

The curvature of the signal can be estimated using the second-order central finite difference approximation [36] with three data points:

$$\left. \frac{\partial^2 E}{\partial b_d^2} \right|_{b_d=b} \approx \frac{E|_{b_d=b-\Delta b_d} - 2E|_{b_d=b} + E|_{b_d=b+\Delta b_d}}{\Delta b_d^2} \tag{2.53}$$

Higher-order approximations and curve fitting could reduce truncation error but require more experimental data [11]. The second-order finite difference approximation effectively minimizes the required data points for estimating the curvature. Therefore, using equations 2.52 and 2.53, f can be measured with as few as four data points per t_m if D_a and D_b are known (D_a and D_b can be esimated by fitting a bi-exponential attenuation model to the experimental data measured with $b_1 = 0$ and varied b_2). One data point at $b_s = 0$ for signal normalization and three data points along a slice of constant b_s for calculating the curvature.

To optimize SNR, the curvature is estimated with $b = 0$ and $\Delta b_d = b_s$ [37]. Furthermore, b_s can be chosen to achieve the greatest curve depth of the signal according to [11]:

$$\underset{b_s \in [0, \infty)}{\arg\max} E(b_s, \pm b_s) - E(b_s, 0) = \ln \left[\frac{D_s}{D_a} + \sqrt{\left(\frac{D_s}{D_a}\right)^2 - 1} \right] \frac{1}{D_d} \tag{2.54}$$

In the curvature method, f is modeled using the same principles as presented in section 2.3.2, and is given by:

$$f(t_m) = \frac{\alpha}{k}(1 - e^{-kt_m}) \tag{2.55}$$

where

$$\alpha = 2f_a k_{ab} = 2f_b k_{ba} \tag{2.56}$$

With experimental data, the exchanging population f at each t_m can be calculated using equations 2.52 and 2.53. Equation 2.55 is then fitted to the calculated $f(t_m)$ to estimate k and α [11].

2.3.5 DEW Model

The DEW model assumes that the extracellular diffusion is free and the intracellular diffusion is restricted by semipermeable boundaries. Diffusion attenuation is expressed using q instead of b under the short gradient pulse approximation, in which diffusive motion during the application of diffusion gradients (i.e., $\delta \ll \Delta$) is neglected. The expression of DEW signal attenuation, which is similar to the DEXSY signal expression (equation 2.26), is also

a population-weighted contribution of all sub-assembles. For a two-compartment exchange system, the normalized attenuation is given by [8]:

$$
\begin{aligned}
E(q) =&P_a' \left[(P_a - P_{ab})e^{-q^2 D_a' \Delta} + P_{ba}e^{-q^2 D_b' \Delta} \right] e^{-q^2 D_a' \Delta} + \\
&P_b' \left[(P_b - P_{ba})e^{-q^2 D_b' \Delta} + P_{ab}e^{-q^2 D_a' \Delta} \right] e^{-q^2 D_b' \Delta}
\end{aligned}
\tag{2.57}
$$

where P_a' and P_b' are the population fractions of intra- and extracellular compartments, respectively. D_a' and D_b' are the apparent diffusion coefficients of the corresponding compartments. It is important to note that the fractional population and the apparent diffusion coefficient depend on q and real biophysical parameters (i.e., the intrinsic diffusion coefficient D and the mean residence time τ). The expressions for P_a', P_b', D_a' and D_b' are given as follows [31]:

$$
P_a' = P_b + \widehat{P}_a - \frac{D_b P_b - D_a P_b - D_a' \widehat{P}_a}{D_b' - D_a'}
\tag{2.58}
$$

$$
P_b' = \frac{D_b P_b - D_a' P_b - D_a' \widehat{P}_a}{D_b' - D_a'}
\tag{2.59}
$$

$$
D_a' = \frac{1}{2} \left\{ D_b + \frac{1}{q^2}\left(\frac{1}{\tau_a} + \frac{1}{\tau_b} \right) - \sqrt{ \left[D_b - \frac{1}{q^2}\left(\frac{1}{\tau_a} - \frac{1}{\tau_b} \right) \right]^2 + \frac{4}{q^4 \tau_a \tau_b} } \right\}
\tag{2.60}
$$

$$
D_b' = \frac{1}{2} \left\{ D_b + \frac{1}{q^2}\left(\frac{1}{\tau_a} + \frac{1}{\tau_b} \right) + \sqrt{ \left[D_b - \frac{1}{q^2}\left(\frac{1}{\tau_a} - \frac{1}{\tau_b} \right) \right]^2 + \frac{4}{q^4 \tau_a \tau_b} } \right\}
\tag{2.61}
$$

where P_a and P_b are the relative populations (constant) in two sites, which are related by $P_a + P_b = 1$. D_a and D_b stand for the intrinsic diffusion coefficients, which are the "true" diffusion coefficients but not the apparent diffusion coefficient extracted from the acquired signal. τ_a and τ_b are the mean residence times in each compartment. $\widehat{P}_a$ is the initial condition for the signal intensity of the intracellular compartment, defined by equation 2.62, in which the effect of restricted diffusion within a sphere is introduced [31].

$$
\widehat{P}_a = P_a \left(\frac{3j_1(qr)}{qr} \right)^2 = \frac{9P_a}{(qr)^2} \left(\frac{\sin(qr)}{(qr)^2} - \frac{\cos(qr)}{qr} \right)^2
\tag{2.62}
$$

Equation 2.62 models a cell as a sphere with radius r, and $j_1(x)$ is the first order spherical Bessel function of the first kind. In this case, a long time limit is assumed, which means the condition $D_a \Delta \gg r^2$ holds. Therefore, the signal within the intracellular space is approximated as $(3j_1(qr)/qr)^2$, which is the first term of the complete intracellular signal attenuation expression. The physical meaning of the approximate expression is that, when diffusion time is long enough (i.e., $D_a \Delta \gg r^2$), the signal attenuation within the cell is not dependent on diffusion coefficient but primarily on the cell size.

Returning to the DEW signal attenuation in equation 2.57, the mixing time t_m is introduced through the parameters P_{ab} and P_{ba}, defined by equations 2.63 and 2.64, respectively [8]. P_{ab} represents the population exchange from a to b, and P_{ba} is the exchanging population in the reverse direction.

$$
P_{ab} = P_a(1 - e^{-t_m/\tau_a})
\tag{2.63}
$$

$$
P_{ba} = P_b(1 - e^{-t_m/\tau_b})
\tag{2.64}
$$

In the DEW experiment, a literature value of the cell radius was used for the exchange estimation. The above equations can be fitted into experimental data to estimate P_a, D_a, D_b, τ_a and τ_b.

2.4   Physical Phantoms

Yeast cell suspensions are well-characterized phantoms used in diffusion MR experiments to measure micro-structural properties, such as the exchange rate and diffusion coefficient. This type of phantom provides a natural two-compartment system with isotropic diffusion in both sites. Furthermore, the yeast suspension phantom is cheap, easily obtainable and reproducible [38]. The typical radius of yeast cells has been reported to be 2.5 μm [39]. Furthermore, a previous study [10] has reported that, at room temperature, the yeast cells have an intracellular diffusion coefficient in the range of 0.037 $\mu m^2/ms$, an extracellular diffusion coefficient of 1.69 $\mu m^2/ms$ with an intracellular fraction of 0.25, and effective exchange rate of 4.4 /s.

3 Method

This chapter introduces the MR scanner on which the exchange measurement experiment was performed, and describes all the procedures applied to carry out the experiment and analyze the acquired data. The procedures include the phantom preparation, the modification of the acquisition sequence, the setting of the acquisition parameters, the dataset selection and the implementation of the estimation processes in each exchange model to obtain the exchange parameters.

3.1 Research MRI System

Experiments for this thesis work were performed using a research benchtop MRI system (Pure Devices, Rimpar, Germany), which is installed in the Lab BRAGG at the Department of Biomedical Engineering of Linköping University, Sweden. As shown in figure 3.1, the MRI system consists of three components: the control unit "drive L", the permanent magnet "magspec", and the gradient amplifier "DC-600". The main technical specifications for the MRI system are listed in table 3.1 [40, 41, 42].

Table 3.1: Main technical specifications of the research MRI system.

Technical Specifications	Values
Field strength	0.55 T
^{1}H frequency	23.5 MHz
Gradient strength (built-in)	x,y: 0.27 T/m; z: 0.38 T/m
Gradient strength (external amplifier)	x,y: 1.2 T/m; z: 1.5 T/m
Bore size	10 mm

The control unit connects the magnet and the gradient amplifier to a computer, on which an interface "openMATLAB" is installed to control the MRI system. The openMATLAB interface is a set of MATLAB libraries provided by Pure Devices. The MR sequence used in the experiment was implemented with the openMATLAB interface (MATLAB R2019b). All the gradient orientations described for the experiment are according to the coordinate system
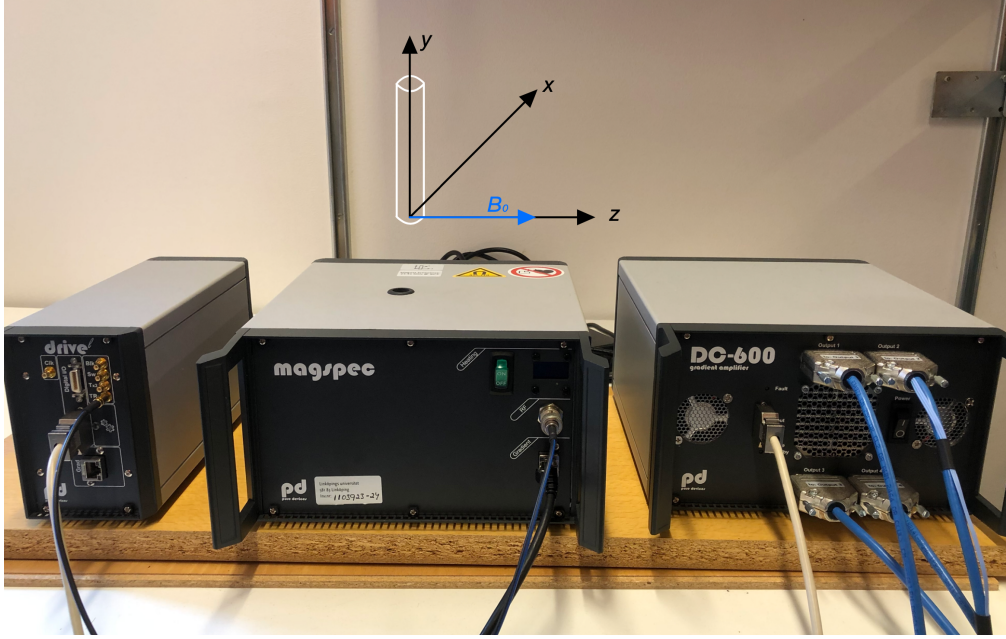
Figure 3.1: Research MRI system setup: the control unit "drive L" (left), the magnet unit "magspec" (middle), and the gradient amplifier "DC-600" (right). The coordinate system specifies the orientation of the linear gradient system of the magnet. The sample bore is along y-axis and the static magnetic field (B_0) is along z-axis.

of the MR scanner as shown in figure 3.1. Furthermore, the magnet temperature was maintained constant at 30 °C while running the experiment. Due to the gradient amplifier, the MRI system can obtain stronger gradient amplitudes than its built-in gradient strength.

3.2   Yeast Phantom Preparation

The water exchange experiment was performed on a yeast phantom. Fresh baker's yeast (Jästbolaget AB, Sweden) was first suspended in ultrapure water with a weight ratio of 3:1 (yeast to water). The yeast suspension was then mixed with a vortex and transferred to a 10 mm outer diameter disposable tube. To form a packed cell sediment, the tube was centrifuged and the supernatant (the liquid above the sediment) was removed. Before being placed in the MR scanner, the yeast phantom was left at room temperature overnight.

In order to observe the yeast cells and estimate their average radius, a picture of the yeast cells was obtained with the use of an inverted microscope (Olympus CKX53). The yeast cells were from the same yeast suspension prepared for MR scans. Before observation under the microscope, the yeast suspension was diluted with ultrapure water in a 1:20 ratio.

The radius of the yeast cells is required in the DEW method to calculate the initial conditions of the intracellular signal attenuation as presented in section 2.3. The radius estimation was performed using image analysis with MATLAB R2020b. The yeast cells were first segmented using edge detection and morphological processing [43]. Then, the image area (the number of pixels) of each yeast cell and the total number of the yeast cells were obtained using the *bwconncomp* function in MATLAB. In the DEW framework, the intracellular diffusion is assumed to be restricted within a sphere. Consequently, the yeast cells can be seen as circles in

the microscope image. Thus, the average radius $\bar{r}$ can be roughly calculated by:

$$\bar{r} = \frac{l}{n} \sum_{i=1}^{n} \sqrt{\frac{Area_i}{\pi}} \qquad (3.1)$$

where n is the number of yeast cells, and $Area_i$ is the number of pixels of the ith yeast cell in the image. The quantity l is the actual length per pixel in the image, which can be obtained by dividing the scale bar label by the length of the scale bar on pixels in the image. The unit of the calculated radius is the same as the unit of the scale bar label.

A structural image of the yeast phantom was acquired using a T_1-weighted spin-echo sequence prior to the water exchange measurement to ensure that no air bubble was present in the selected slice of the yeast phantom. The water exchange scan was performed in the same slice as the structural scan with identical slice selection parameters. The voxel size of the structural image is $0.078 \times 0.078 \times 6$ mm^3. In order to improve the SNR, five identical measurements were performed and the average of them was taken.

3.3 Acquisition Sequence

The sequence used for measuring exchange is based on the aforementioned double diffusion sequence employed in the DEXSY experiment. The sequence was modified from a previously implemented FEXI sequence on the benchtop MR scanner [44]. In the FEXI sequence, the gradients of the first diffusion encoding block are fixed to one value during scanning. Therefore, in order to acquire a 2D dataset, the two pairs of diffusion gradients were modified to vary independently using the openMATLAB libraries.

The modified sequence is shown in figure 3.2, where the slice selection gradients are applied in the y-axis, and the frequency encoding diffusion gradients are applied in the z-axis. The phase encoding gradients were not used in the experiment, and thus a 1D image of the yeast sample was acquired along the frequency encoding direction. The acquisition time can be reduced significantly without the application of phase encoding. This 1D image acquisition scheme is valid in this study since the measured yeast sample is nearly homogeneous and is not expected to exhibit voxel-to-voxel variations.

Two groups of spoiler gradients were applied to dephase the unwanted echoes. The first group of spoilers (A) was used during the mixing time in each direction. These spoilers remove the residual transverse magnetization during the mixing time. The second group of spoilers (B) was modified from the implementation presented in the DEW sequence [8]. These spoilers are a pair of gradients applied in the y-axis before the application of the second 90° RF pulse and after the third 90° RF pulse. This pair of spoilers were used to dephase the undesired magnetization excited by the third 90° RF pulse and keep the magnetization weighted by the first diffusion and exchange blocks. The spoilers are applied along the slice selection direction since the spoilers exhibit more phase dispersion efficiency along this direction [8].
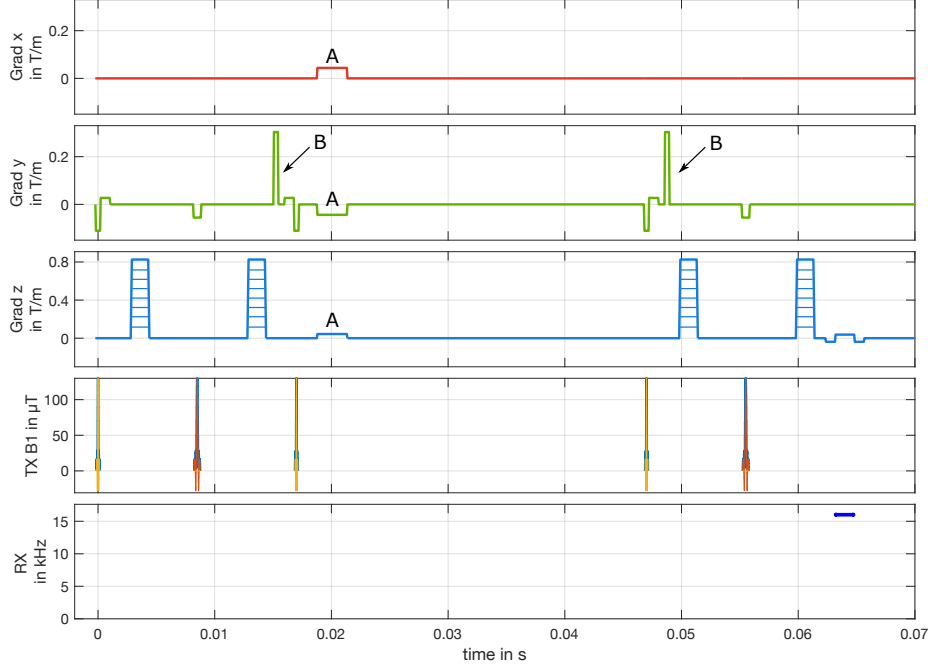
Figure 3.2: Sequence implemented on the MR scanner to measure exchange. Phase encoding gradients were not applied to reduce the acquisition time. Spoilers A and B are employed to suppress the remaining transverse magnetization during the mixing time and retain the diffusion-exchange-weighted magnetization, respectively. The acquired signal is indicated in the RX channel.

3.4 Acquisition Parameters

The acquisition parameters used for the water exchange measurement are listed in table 3.2. The time parameters of each diffusion encoding block were kept constant for all acquisitions. With $\Delta = 10$ ms, the condition $\Delta \ll 1/k = 285$ ms is met ($k = 3.5$ /s was used, as reported in [9]), fulfilling the assumption that exchange only occurs during the mixing time and not during the diffusion encoding blocks. Diffusion encoding was applied in the z-axis with b_1 and $b_2 = 0$ - 1.2 ms/µm^2 in 17×17 (b_1 ,b_2) steps at each mixing time. The values of b_1 and b_2 are linearly spaced between 0.02 to 1.2 ms/µm^2 (16 points). Note that five additional acquisitions with $b_1 = 0$ and b_2 in the range 1.28 - 2.0 ms/µm^2 were applied to increase the number of samples used to measure D_a and D_b for the curvature method, which will be presented in the next section. The measurement was performed with ten different $t_m = 10, 30, 50, 70, 90, 110, 130, 150, 250$ and 350 ms. The values of mixing time were not increased any further to avoid a great attenuation of the acquired signal due to T_1 relaxation. Similarly, TE was kept short to limit the effect of T_2 relaxation. The experiment was repeated five times and averaged to achieve a higher SNR.

Table 3.2: Acquisition parameters used for exchange measurement on the yeast phantom.

Parameters	Values
δ (ms)	1.5
Δ (ms)	10
ε (ms)	0.1
b_1 (ms/µm^2)	0 - 1.2 (#17)
b_2 (ms/µm^2)	0 - 1.2 (#17)
when $b_1 = 0$	0 - 2.0 (#22)
t_m (ms)	10 - 350 (#10)
TE (ms)	17
TR (ms)	1200
FOV (mm^2)	10
Slice thickness (mm)	6
Matrix size	1×24
Diffusion direction	z-axis
Number of averages	5

3.5 Data Selection and Exchange Estimation

The four models presented in section 2.3 were implemented to measure exchange in this thesis work. Each mathematical model was fitted to the experimental data along its own trajectory to obtain the exchange parameters. The general model was used to fit the full space data and each sub set of the data along each reduction trajectory to estimate exchange. A shifted DEW trajectory and a new trajectory were proposed as new subsampling schemes used in the general model to measure exchange. All the fits were performed using a non-linear least-squares algorithm that was implemented using the *lsqcurvefit* function in MATLAB R2020b. The exchange parameters which require to be estimated in each model are listed in table 3.3. The initial value of the same parameter was set to be the same for all the fitting processes.

Table 3.3: Unknown exchange parameters in each model.

Models	Parameters
General model	$k, D_a, D_b, f_a, T_1, S_0$
FEXI model	$AXR, ADC_{eq}, \sigma, T_1, S_0$
Curvature model	$k, \alpha, D_a, D_b, f_a, S_0(t_m)$
DEW model	$\tau_a, \tau_b, D_a, D_b, P_a, T_1, S_0$

The exchange results obtained using the general, FEXI and curvature models are compared with each other since the three of them follow the free diffusion assumption. The result of the DEW method provides the exchange information of restricted diffusion. Residuals of each estimation method were computed and compared to assess the goodness of each fit. The squared residual R^2 was used in this study and is given by:

$$R_i^2 = \left(\frac{S_i - \hat{S}_i}{S_i} \right)^2 \tag{3.2}$$

where S_i is the measured signal intensity of the ith sample and $\hat{S}_i$ its estimated signal intensity.

3.5.1 Data Selection for Each Model

The dataset used for the fit was extracted from the acquired signal at with *b-values* ranging from 0.02 to 1.04 ms/μm^2 for each mixing time. Data with higher *b-values* were discarded to ensure that the signal used for estimation has a relatively good SNR. The threshold value was determined by observing the histogram of the signal intensity.

Two criteria were set to achieve a fair comparison between each model since each one uses different subsampled datasets for estimation. The subsampled datasets used for each model were supposed to have the same (or similar) number and range of *b-values*. In this study, the number of samples per mixing time was set as 14 and the range of *b-values* is 0.02-1.04 ms/μm^2 as mentioned before.

The samples used in each model are shown in figure 3.3. The full space dataset (size: 14 × 14 × 10 ($b_1 \times b_2 \times t_m$)) was analyzed using the general model to provide the "ground truth" of the exchange parameters for the data reduction methods except for the DEW method. The subsampled FEXI, curvature and DEW datasets were used in their corresponding models and the general model to estimate exchange parameters.
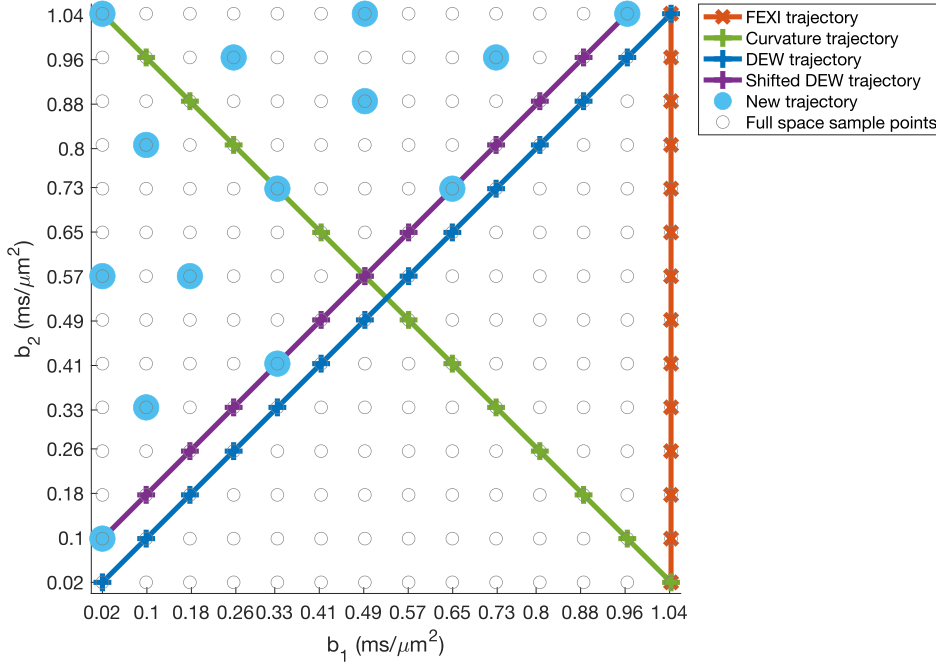
Figure 3.3: Subsampled experimental dataset used in each model to estimate exchange. The experimental dataset is a 3D dataset since measurements were repeated at each mixing time. This figure does not illustrate the mixing times. Samples in the full space are represented by blank circles. The FEXI acquisition trajectory is labeled with a red line with $b_1 = 1.04$ ms/μm^2 and 14 varying b_2 values, the curvature samples are along a slice of constant $b_s = 1.06$ ms/μm^2, which is illustrated by a green line, the DEW samples are along the diagonal as colored with blue, the shifted DEW trajectory is labeled with a purple line, and the samples in the new trajectory are colored with cyan. The number of samples along each trajectory is 14 except for the shifted DEW trajectory, which has 13 samples.

Two new subsampling schemes were proposed. One is the shifted DEW trajectory, which is parallel to the DEW acquisition trajectory. The shifted DEW trajectory has increasing $b_1 + b_2$

and constant $b_2 - b_1$. The second new trajectory consists of uniformly distributed sample points in half of the data plane separated by its diagonal. The new trajectory was inspired by the symmetry property of the signal presented in the curvature framework. Recalling this property in section 2.3, at steady state, the signal intensity is symmetric about the diagonal. The samples above (or below) the diagonal could theoretically represent the full space samples and thus can be used as a sample reduction method. The general model was fitted to the samples along with the shifted DEW and new trajectories for estimating exchange.

3.5.2 General Model Estimation

The general mathematical model used for the fit accounts for the T_1 relaxation during the mixing time to separate the dependency of the mixing time from the original signal S_0. The general model is presented in equation 3.3 (based on equation 2.38), where the unknown parameters are k, D_a, D_b, f_a, T_1 and S_0 as listed in table 3.3. It should be noted that equation 3.3 is based on the assumption that T_1 for both compartment is identical or similar.

$$
\begin{aligned}
S(b_1, b_2, t_m) =& S_0 e^{-t_m/T_1} \{ e^{-b_2 D_a} [f_a e^{-b_1 D_a} + f_a(1-f_a)(e^{-b_1 D_b} - e^{-b_1 D_a})(1 - e^{-kt_m})] + \\
& e^{-b_2 D_b} [(1-f_a)e^{-b_1 D_b} + f_a(1-f_a)(e^{-b_1 D_a} - e^{-b_1 D_b})(1 - e^{-kt_m})] \}
\end{aligned}
\tag{3.3}
$$

In order to ensure the estimated results using different models are comparable, the parameter ADC_{eq} in the FEXI model can be calculated using the parameters estimated in the general model via:

$$
ADC_{eq} = f_a D_a + (1 - f_a) D_b
\tag{3.4}
$$

3.5.3 FEXI Model Estimation

Recalling the FEXI signal attenuation presented in equation 2.42, $S_f(t_m)$ comprises the effects of the application of the filter block and T_1 relaxation during the mixing time. Consequently, by expressing the signal decay due to the filter block and T_1 relaxation and incorporating $ADC'(t_m)$ in equation 2.45 to equation 2.42, a global mathematical expression of FEXI attenuation can be obtained by:

$$
\begin{aligned}
S(b_1, b_2, t_m) =& S_f(t_m) e^{-ADC'(t_m)b_2} \\
=& S_0 e^{-t_m/T_1} e^{-b_1 ADCeq} e^{-b_2 ADC_{eq}(1 - \sigma e^{-AXRt_m})}
\end{aligned}
\tag{3.5}
$$

The unknown exchange parameters for the FEXI global estimation are AXR, ADC_{eq}, σ, T_1 and S_0 as listed in table 3.3. A vertical slice of the experimental dataset (figure 3.3) was fitted into equation 3.5 to estimate the exchange parameters.

3.5.4 Curvature Model Estimation

The curvature estimation was implemented in three steps. Firstly, D_a, D_b and $S_0(t_m)$ were estimated. As presented in section 2.3, D_a and D_b are known prior to the exchange measurement. These parameters were obtained by fitting a bi-exponential diffusion attenuation model to the experimental signal measured at $t_m = 10$ ms and with $b_1 = 0$ and 21 b_2 values ranging from 0.02 to 2.0 ms/µm². This is due to the applied double diffusion encoding sequence with $b_1 = 0$ and varied b_2 can be seen as a 1D diffusion measurement. Note that the number of samples used for the bi-exponential estimation is not required to satisfy the comparison criteria (where the number is 14) since D_a and D_b are treated as prior knowledge to the exchange system in the curvature experiment. On the other hand, with b up to 1.04 ms/µm², the measured signal only attenuates approximately 40% in this "single PGSE" experiment, resulting in inaccurate D_a and D_b being estimated. Therefore, more samples with

higher *b-values* are used for this estimation. The bi-exponential attenuation model is presented in equation 3.6. D_a and D_b were then used to calculate D_d and D_s (equation 2.49) for estimating the exchanging fraction in the next step.

$$S(b_2, t_m) = S_0(t_m)[f_a e^{-b_2 D_a} + (1 - f_a)e^{-b_2 D_b}] \tag{3.6}$$

Furthermore, by repeating the fit to the experimental data with $b_1 = 0$ and varying b_2 (0.02 - 2.0 ms/µm²) for the remaining nine mixing times, the original signal S_0 at each mixing time was obtained. S_0 was provided for signal normalization which was used in the second step to calculate the exchanging fraction. The method used in this thesis work to obtain $S_0(t_m)$ is different from the original curvature experiment, in which $S_0(t_m)$ is the signal directly acquired with $b_1 = b_2 = 0$ at each mixing time but not the estimated signal. The experimental $S_0(t_m)$ was not used in this thesis work since it would introduce more voxel-to-voxel variations. Note that the experimental data used to estimate D_a, D_b and $S_0(t_m)$ were obtained from the same acquisition used for measuring exchange, and equation 3.6 is valid if T_1 and T_2 of each compartment are assumed to be similar.

Secondly, the exchanging fraction f was calculated at each mixing time. This was done by estimating the curvature $\partial^2 E/\partial b_d^2$ and then substituting D_s, D_b and the corresponding estimated curvature into equation 2.52. The curvature at each mixing time was estimated using a second-order polynomial fit with 14 samples along with the trajectory of constant $b_s = 1.06$ ms/µm², as shown in figure 3.3. The three-point finite difference approximation was not applied since the number of samples in each estimation should be the same. The sample's signal intensity at each mixing time for estimating the curvature was normalized with $S_0(t_m)$ obtained in the first step.

Thirdly, the exchange rate was obtained by fitting equation 2.55 to the exchanging fractions calculated in the second step. The curvature framework provides a different scheme to estimate exchange. Instead of directly fitting a signal attenuation model to the experimental signal, the framework estimates the exchange rate by fitting an exchanging fraction recovery model to the exchanging fractions calculated by the estimated signal curvature.

The curvature estimation does not directly provide the residuals of signal intensity. The estimated signal intensity in the curvature model was calculated using the estimated parameters and the signal decay expression as presented in equation 3.7. The parameters $S_0(t_m)$, f_a, D_a and D_b were estimated using the bi-exponential attenuation model, and consequently, D_s and D_d were calculated from D_a and D_b as mentioned before. The estimated exchanging fraction f was obtained in the fit described in the third step. Substituting the above estimated parameters into equation 3.7, the signal intensity of the curvature model was estimated.

$$S(b_s, b_d, t_m) = S_0(t_m)[(f_a - \frac{f}{2})e^{-b_s D_a} + (1 - f_a - \frac{f}{2})e^{-b_s D_b} + f e^{-b_s D_s} \cosh(b_d D_d)] \tag{3.7}$$

3.5.5 DEW Model Estimation

In the DEW model, the signal intensity is expressed as a function of q instead of b. Recalling the definition of q presented in section 2.2, for the trapezoidal pulses used in this work, $q = \gamma \delta G$, where G can be calculated using b and other experimental time parameters by equation 2.18. Accordingly, q can be obtained by:

$$q = \sqrt{\frac{b}{\Delta - \frac{\delta}{3} + \frac{\varepsilon^3}{30\delta^2} - \frac{\varepsilon^2}{6\delta}}} \tag{3.8}$$

The radius of yeast cells was estimated using the image analysis method presented in section 3.2. Similarly to the aforementioned general and FEXI estimations, the DEW model also

accounts for the T_1 relaxation during the mixing time. The signal attenuation expression applied for the fit that incorporates this is given by equation 3.9. The exchange parameters were estimated by performing a global fit of equation 3.9 with equations 2.58, 2.59, 2.60, 2.61, 2.62, 2.63 and 2.64 presented in section 2.3 to the experimental data acquired along the DEW trajectory (figure 3.3).

$$S(q, t_m) = S_0(e^{-t_m/T_1})\{P_a'[(P_a - P_{ab})e^{-q^2 D_a' \Delta} + P_{ba}e^{-q^2 D_b' \Delta}]e^{-q^2 D_a' \Delta} +$$
$$P_b'[(P_b - P_{ba})e^{-q^2 D_b' \Delta} + P_{ab}e^{-q^2 D_a' \Delta}]e^{-q^2 D_b' \Delta}\} \tag{3.9}$$

The estimated values are τ_a, τ_b, D_a, D_b, P_a, T_1 and S_0. The exchange rate (k) was calculated using the mean residence time ($\tau_{a,b}$) of each compartment by equation 3.10.

$$k = \frac{1}{\tau_a} + \frac{1}{\tau_b} \tag{3.10}$$

4 Results

This chapter outlines the results of the phantom preparation, data acquisition and estimation of exchange parameters using the four models in this study.

4.1 Yeast Phantom

Figure 4.1a shows a microscopy image of the yeast cells. The scale bar label is 20 μm in the microscope image. As shown in figure 4.1b, the yeast cells used for calculating the average radius are colored with magenta. The estimated average radius for the yeast cells is 2.82 μm.

Structural images of the yeast phantom are presented in figure 4.2. Figure 4.2a shows an image of the yeast phantom without air bubbles in the selected slice acquired prior to water exchange measurements. No air bubbles were observed in the sample after the full acquisition protocol. For comparison, figure 4.2b clearly shows the presence of air bubbles in the selected slice of a yeast sample. This image was acquired after measuring water exchange in a pre-experiment in which the scanned yeast sample had not been centrifuged.
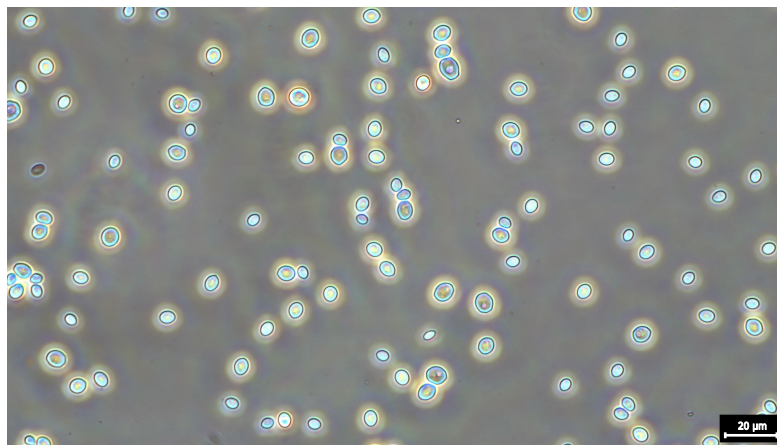
(a) The original microscopy image of the yeast cells.
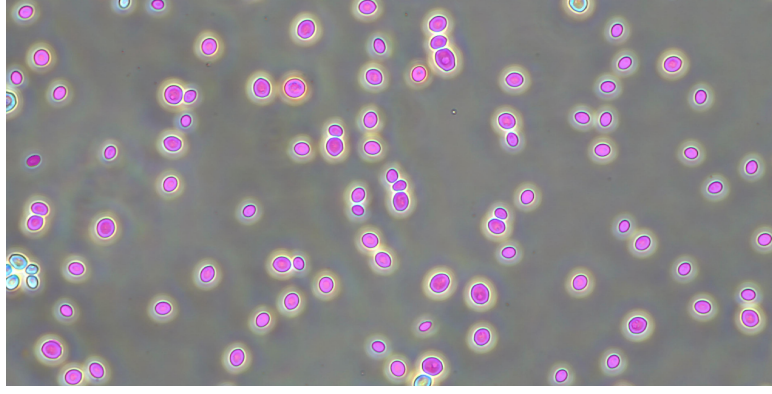
(b) Yeast cells overlaid with magenta were used for radius estimation.

Figure 4.1: Yeast cells observed under a microscope. The sample was diluted with ultrapure water before observation under the microscope.

(a) Without air bubbles

(b) With air bubbles

Figure 4.2: Structural images of the yeast phantom (a) without air bubbles and (b) with air bubbles.

4.2 Exchange Result

The estimated parameters from the four exchange models are presented and compared in this section. Fits obtained from the four models to the corresponding dataset were plotted for the center (12th) voxel of the yeast 1D image for visibility. In order to compare the fits of the same dataset performed by different models in one pl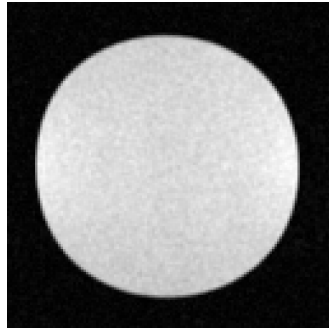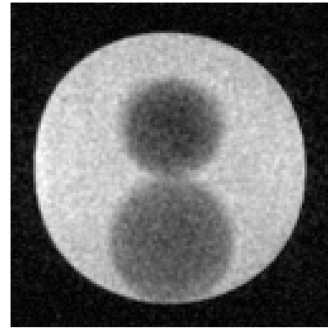ot, the experimental and estimated signals were normalized with the same S_0 and T_1 relaxation during each mixing time. The S_0 and T_1 obtained by fitting the general model to the full space dataset were used for this purpose. The tables of each model's estimated exchange parameters and mean squared residuals (MSRs) are presented at the end of this section. The estimated parameters and calculated residuals were obtained from the data in the region of interest (ROI), which is defined by the center ten voxels (8th - 17th) in the yeast sample 1D image.

4.2.1 Full Space Signal Profile

The experimental and estimated signals as functions of b_1 and b_2 for different mixing times are shown in figure 4.3. The estimated signal was obtained by fitting the general model to the full space dataset. Both experimental and estimated signal intensities were normalized with the estimated S_0 and T_1 relaxation as mentioned before. As can be observed, the estimated signal follows almost the same decay trend as the experimental one. The signal attenuates equally along both b_1 and b_2 at each mixing time. It can be observed that the signal decays

slightly more prominently as the mixing time increases. The experimental signal has more fluctuations at long mixing times (e.g., t_m = 250 ms). Unexpected peaks are observed along the diagonal with $b_1 = b_2$ in the full space signal profiles of the experimental data. The peaks could be artifacts and lower the accuracy of the estimated parameters. Thus, these peaks were excluded from the full space dataset that the general model was fitted to. The exchange parameters estimated from the remaining space are k = 4.9 /s, D_a = 0.064 µm^2/ms, D_b = 1.305 µm^2/ms, and f_a = 0.49, as listed in table 4.1. Note that the "full space dataset" referred in the following context represents the remaining data excluding the peaks.
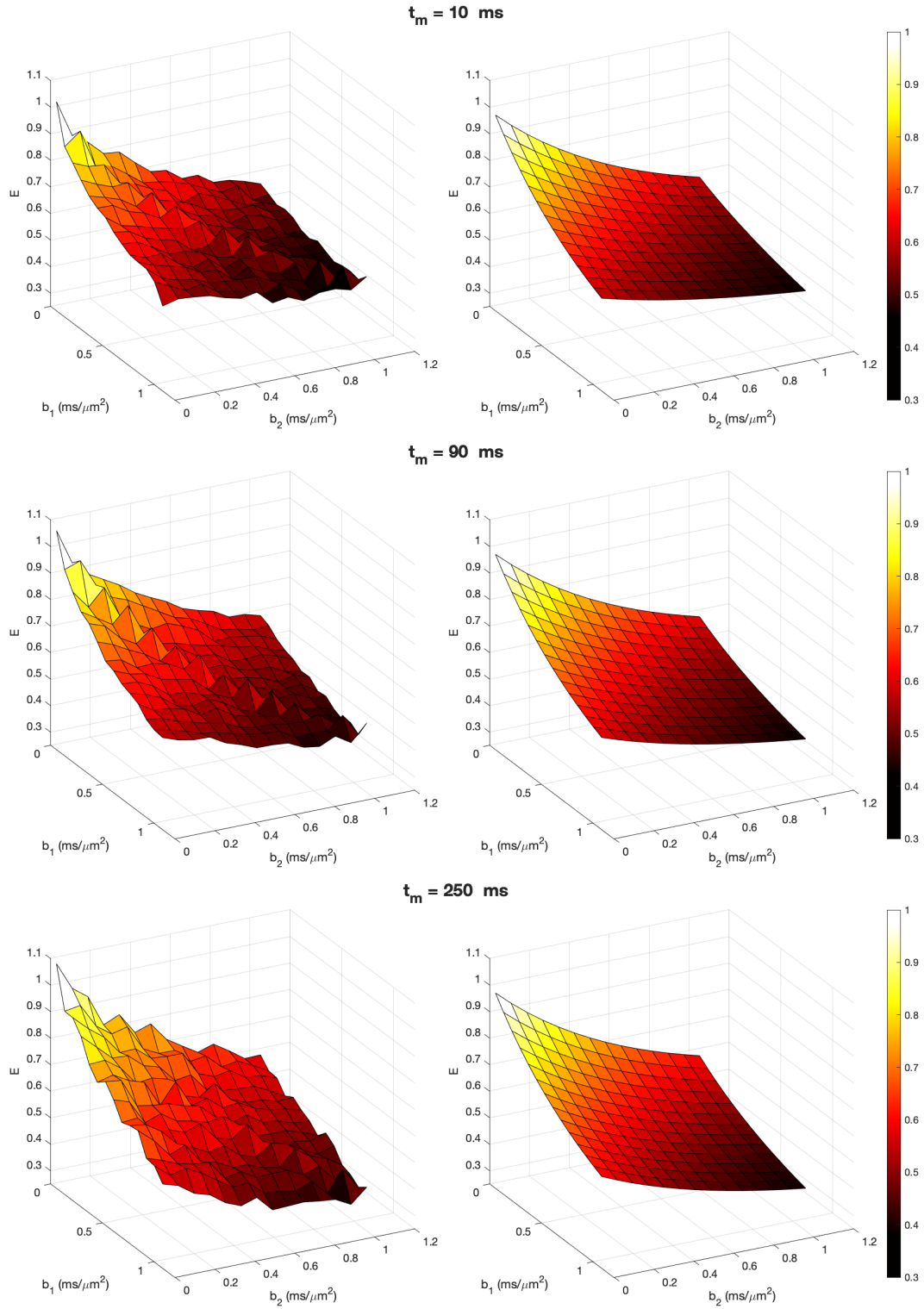
Figure 4.3: Full space signal profiles of the experimental and estimated data at different mixing times. The estimated data were obtained by fitting the general model to the full space dataset (excluding the peaks). Left side: the experimental signal; right side: the estimated signal.

4.2.2 Fits of FEXI Dataset

The fits of the FEXI dataset using the FEXI model and the general model are shown in figure 4.4. The general model fit of the full space dataset is plotted together for comparison. It can be observed that the estimated signal attenuation in this figure is more prominent at longer mixing times than in the full space signal profiles previously presented. This can be explained by the FEXI model (equation 3.5), where $ADC'(t_m)$ increases as t_m increases, and thus the signal intensity as a function of b_2 decays more quickly.
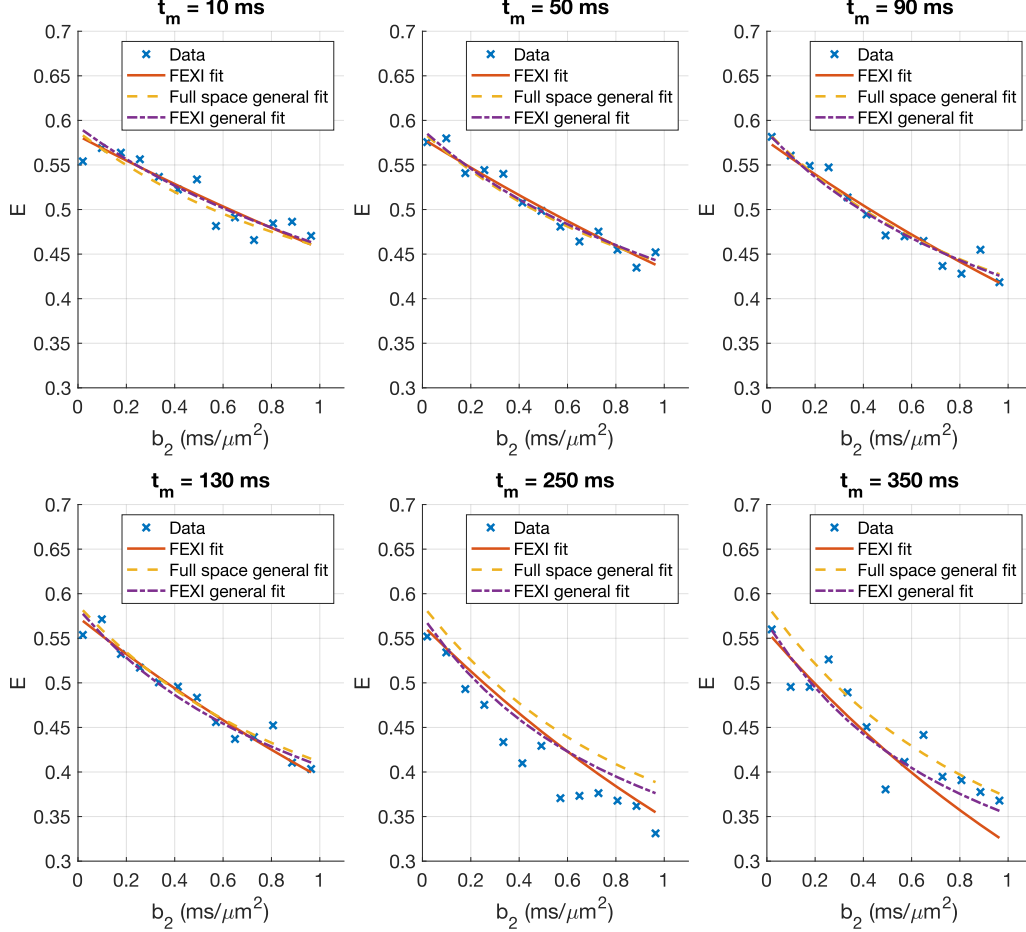
Figure 4.4: Comparison of the FEXI model fit and the general model fit. The figure shows the normalized signal vs. b_2 at constant $b_1 = 1.04$ ms/μm^2 for various mixing times. The experimental data are marked with blue crosses. The FEXI model fit is plotted with solid red lines, the general model fit of the FEXI dataset with dash-dotted purple lines, and the general model fit of the full space dataset with dashed yellow lines. The FEXI model fit curves appear as straight lines since the model is a mono-exponential function with a relatively small exponent parameter ($ADC' \leqslant ADC_{eq} = 0.814 \pm 0.315$ μm^2/ms, as listed in table 3.3) and thus it is not a prominent curve.

The FEXI acquisition trajectory passes through the samples with $b_1 = b_2$, which are the peaks mentioned before. Similarly, these peaks were not included in the FEXI dataset used for estimating the exchange parameters. The three fits yielded very close estimated signals for short mixing times. However, at long mixing times (e.g., $t_m = 250$ ms, 350 ms), the estimated signals can hardly accommodate the trend of the experimental data, and the general model fit of the full space dataset predicts a higher signal intensity than the fits of the FEXI dataset.

This is due to more random variations in the experimental data at long mixing times. The variations lower the estimation accuracy of the FEXI model and the general model fitted to this FEXI dataset to an extent. The general model fit of the full space dataset is less affected by the variations since it accommodates the entire experimental data.

The general model fit of the FEXI dataset yielded k of 4.4 /s, which is close to the exchange rate obtained from the full space dataset. But estimates of both diffusion coefficients are higher. The FEXI model fit gave AXR of 3.2 /s and ADC_{eq} of 0.815 µm^2/ms. Both of them deviate from the estimates from the full space dataset.

4.2.3 Fits of Curvature Dataset

The fit obtained using the bi-exponential decay model is shown in figure 4.5. The model fits the data fairly well, providing relatively accurate D_a and D_b as the prior knowledge for the curvature framework. The signals estimated using the curvature model and the general model are shown in figure 4.6a. The second-order polynomial fits were used to estimate the curvatures of the experimental data. The estimated curvature signal were calculated using the estimated exchange rate and parameters obtained using bi-exponential model as mentioned in 3.5. Residuals of the curvature model were calculated using the estimated signal not the polynomial fitted signal.
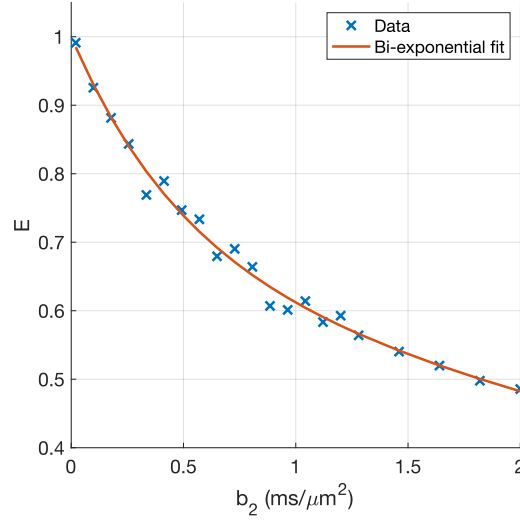
Figure 4.5: Fit of the normalized signal using the bi-exponential model (equation 3.6). The experimental data were measured with varying b_2 values at $b_1 = 0$ and $t_m = 10$ ms. The signal intensity was normalized with the S_0 obtained by the bi-exponential fit.

No clear curvature can be observed in the experimental data since the depth of the signal curve is very shallow and the random variations between the data are even larger than the depth. The shallow curvature and the random variations make the fits difficult to accommodate the trend of the measured signal. As can be observed, the estimated signals in the general model (fitted to the full space dataset) and the curvature model barely fit the experimental data. The polynomial fit does not present a clear increase in the curvature as the mixing time increases. Moreover, at certain mixing times, the middle points (b_d is close to 0) of the experimental data have higher signal intensities than the points on the two sides, resulting in negative curvatures obtained by the polynomial fit and thus negative exchanging fractions. The negative fractions can be observed in figure 4.6c ($t_m = 10$ ms, 250 ms), affecting the accuracy of the estimated exchange rate. The curvature model fit yielded k of 8.99 /s, which is

two times higher than the estimated one from the full space dataset. The general model fit on the curvature dataset greatly deviates from the experimental data and is not illustrated in the figure.

(a) Normalized signal vs. b_d at constant $b_s = 1.06$ ms/µm^2 for various mixing times.

(b) Simulated data

(c) Exchanging fractions vs. t_m.
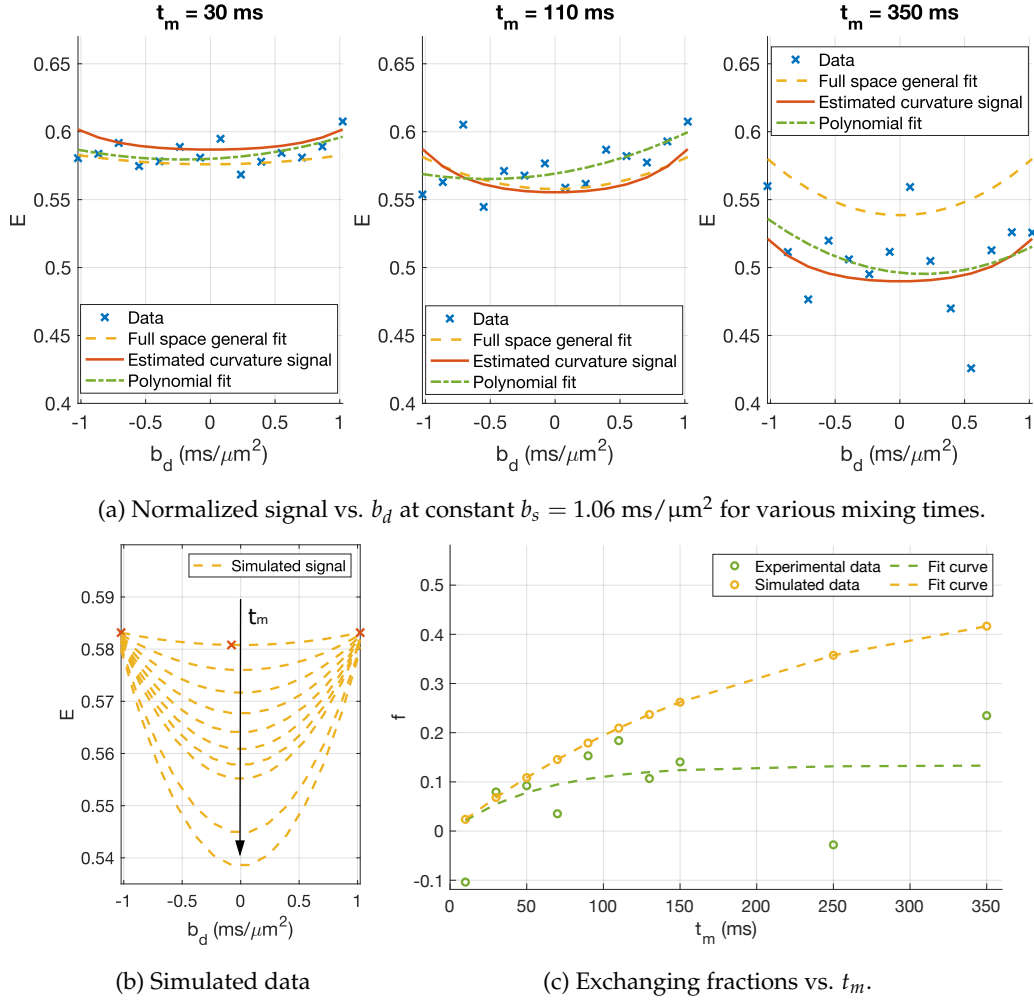
Figure 4.6: Comparison of the curvature model fit and the general model fit. (a): Signal decay at different b_d values and for three different mixing times. Blue crosses: the experimental data; solid red lines: the signal estimated using the curvature model ; dash-dotted green lines: the second-order polynomial fit; dashed yellow lines: the general model fit of the full space dataset. (b): Synthesized data using the estimated parameters with the full space dataset vs. b_d for all the mixing times. The arrow indicates increasing t_m. Points used for curvature estimation by the finite difference approximation are labeled with red crosses (only illustrated for the first t_m). (c): Exchanging fraction recovery curve obtained from the experimental data and the simulated data. Green circles: fractions calculated using the curvature estimated from the polynomial fit in (a); dashed green line: the fitted fraction curve of the calculated fractions; yellow circles: the simulated fractions from (b); dashed yellow line: the fitted fraction curve of the simulated fractions.

Increasing curvatures with the mixing time can be observed in the estimated signal from the general model fit on the full space dataset, as shown in figure 4.6a. For a clearer illustration, the signal synthesized using the general model with the estimated parameters on the full space dataset for different mixing times were plotted together in figure 4.6b. The estimated parameters used for synthesizing the signal are $k = 4.75$ /s, $f_a = 0.50$, $D_a = 0.07$ µm^2/ms and

D_b = 1.34 µm^2/ms. As expected, the signal is symmetric about $b_d = 0$ and the degree of its curvature increases noticeably as the mixing time increases. The synthesized (or simulated) signal were applied to test the validity of the results from the curvature framework. The curvature of the simulated signal was estimated from the second-order finite difference approximation (equation 2.53) with three points at each mixing time. The exchanging fractions were then calculated from the curvatures. The fraction recovery expression (equation 2.55) was finally fitted to the simulated fractions, yielding a fitted fraction increasing with the mixing time (figure 4.6c) and a fitted exchange rate k = 4.75 /s, which is consistent with estimated exchange rate used to synthesize the signal.

4.2.4 Fits of DEW dataset

The fits of the DEW dataset using the DEW model and the general model are shown in figure 4.7. The fit obtained with the general model on the full space dataset is not provided for comparison since the DEW dataset consists of all the peak data points which were not used in the full space estimation. As can be observed, the DEW and general models fit the DEW dataset well at short mixing times. Long t_m introduces more random variations to the experimental data and could affect the accuracy of the fitted parameters. However, the DEW model tries to accommodate the variations, as can be seen by the downward motion of the DEW fitted curve at t_m = 350 ms in figure 4.7. This is an interesting finding and could be explained by the DEW mathematical model, which is a complicated multi-exponential function (equation 2.57). D'_a and D'_b are changing as q increases, providing multiple exponential components. The weighting of some exponential components varies as t_m increases, and thus the fitted curve presents multiple decay trends to fit the experimental data.

Although the full space estimation excluded the DEW data (peaks), the general model fit on the DEW dataset yielded k = 4.43 /s, which is close to the one given by the full space estimation. However, the estimated diffusion coefficients are higher than the full space estimates.
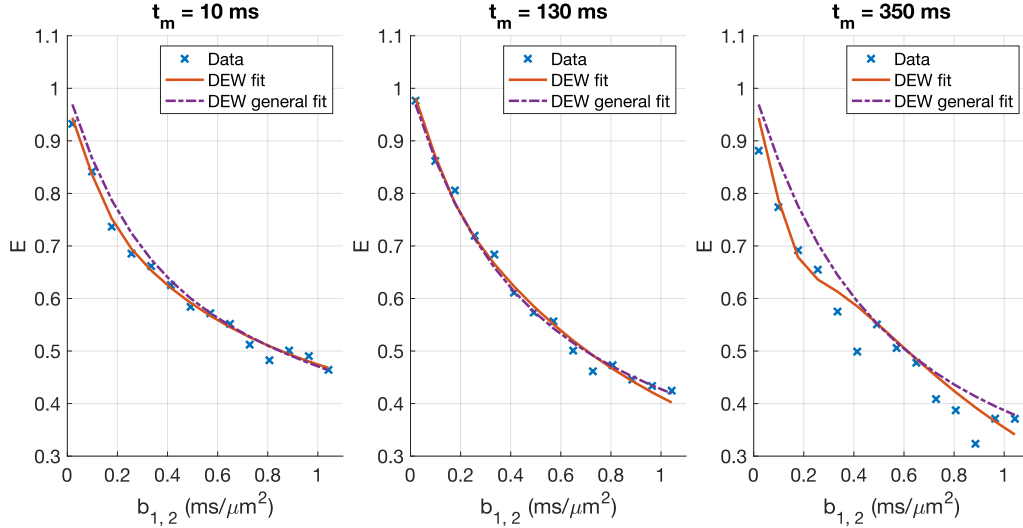
Figure 4.7: Comparison of the DEW model fit and the general model fit. The figure shows the normalized signal vs. $b_{1,2}$ ($b_1 = b_2$) for various mixing times. The signal is normalized with the parameters (S_0 and T_1) obtained from the general model fit on the DEW dataset. The experimental data are marked with blue crosses. The DEW model fit is plotted with solid red lines, and the general model fit of the DEW dataset with dash-dotted purple lines. Both the DEW model and general model fit the data well.

4.2.5 Fits of Shifted DEW and New Trajectory Datasets

The fits of the shifted DEW and full space datasets are illustrated in figure 4.8. Both the fits accommodate the experimental data well except for the data acquired at the longest mixing time. The fitted signals from the two datasets are almost overlapped. The diffusion coefficients obtained from the shifted DEW dataset are consistent with the full space one, as listed in table 4.1. But the exchange rate from this reduced dataset is higher than the full space one.
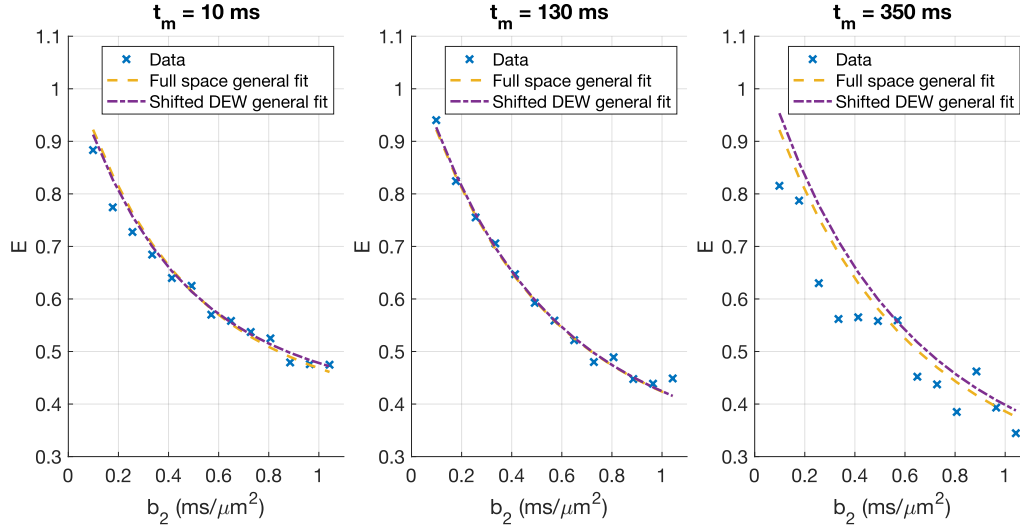
Figure 4.8: Comparison of the fits obtained with the general model for the shifted DEW and full space datasets at different mixing times. The figure shows the normalized signal vs. b_2 in the range of 0.1-1.04 ms/μm^2 (b_1 in the range of 0.02-0.96 ms/μm^2). The experimental data are labeled with blue crosses, the fit of the shifted DEW dataset using the general model is plotted with dash-dotted purple lines, and the fit of the full space data with dashed yellow lines.

The fits of the data acquired along with the new trajectory and of the full space dataset using the general model are shown in figure 4.9. As can be observed, the fitted signals of the new subsampled and the full space datasets are almost consistent with each other. The general model fits the experimental data acquired along with the new trajectory fairly well for short mixing times ($t_m \leqslant 250$ ms). Similar to the shifted DEW dataset, the subsampled dataset along the new trajectory exhibits more random variations at the longest mixing time and the fits predict higher signal intensity. The fit of the subsampled dataset along the new trajectory yielded $k = 5.07$ /s, which is closest to the full space estimate over other methods.
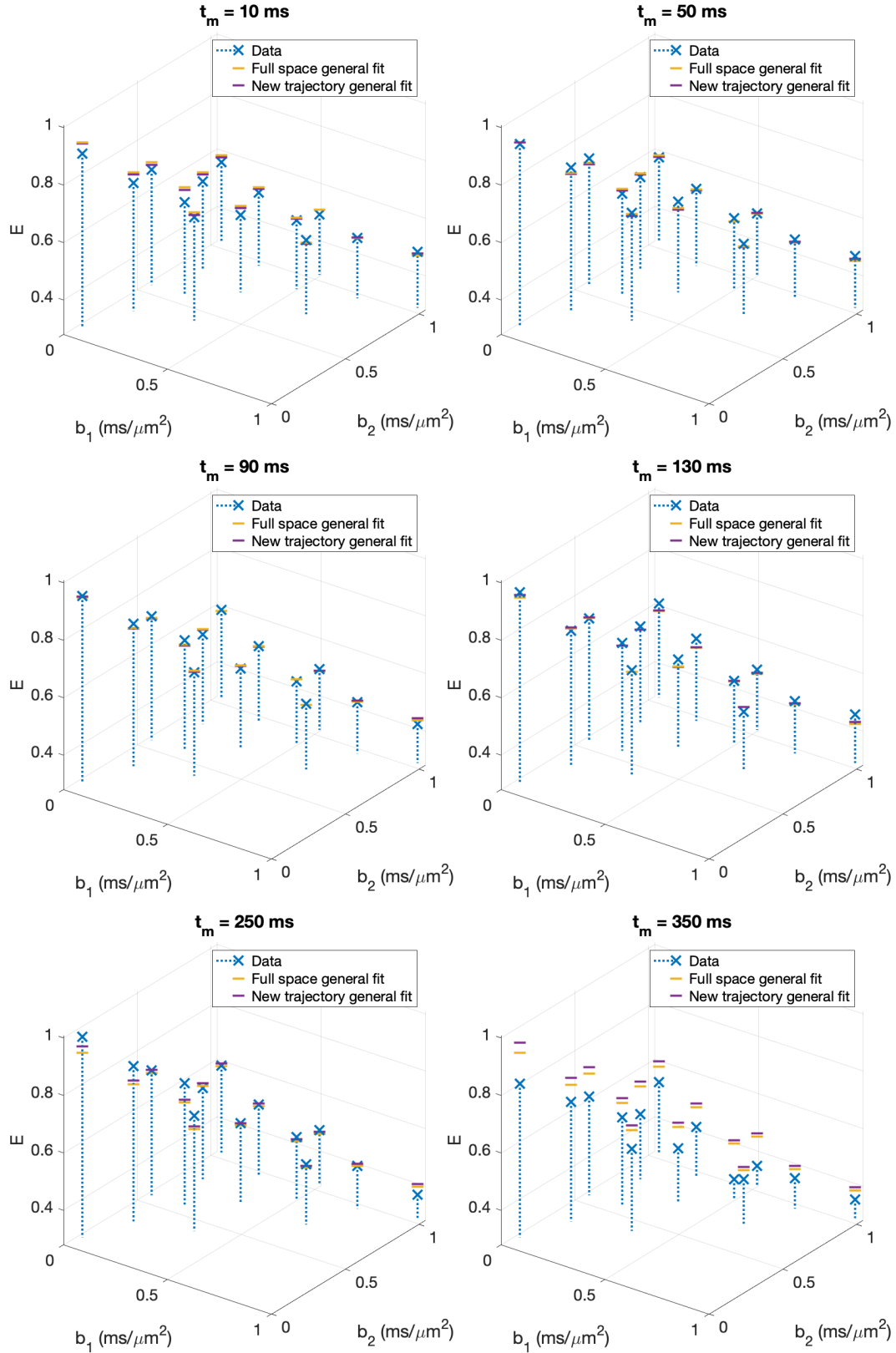
Figure 4.9: Comparison of the fits obtained with the general model to the new trajectory and full space dataset. The figure shows the normalized signal vs. b_1 and b_2. The experimental data are labeled with blue crosses, the fit of the new trajectory dataset using the general model with purple bars, and the fit of the full space data with yellow bars.

4.2.6 Exchange Parameters and Residuals

The exchange parameters estimated using the four models and the corresponding datasets are presented in table 4.1. For better illustration, the error bar plots of the estimates from the models under free diffusion assumption are shown in figure 4.10.
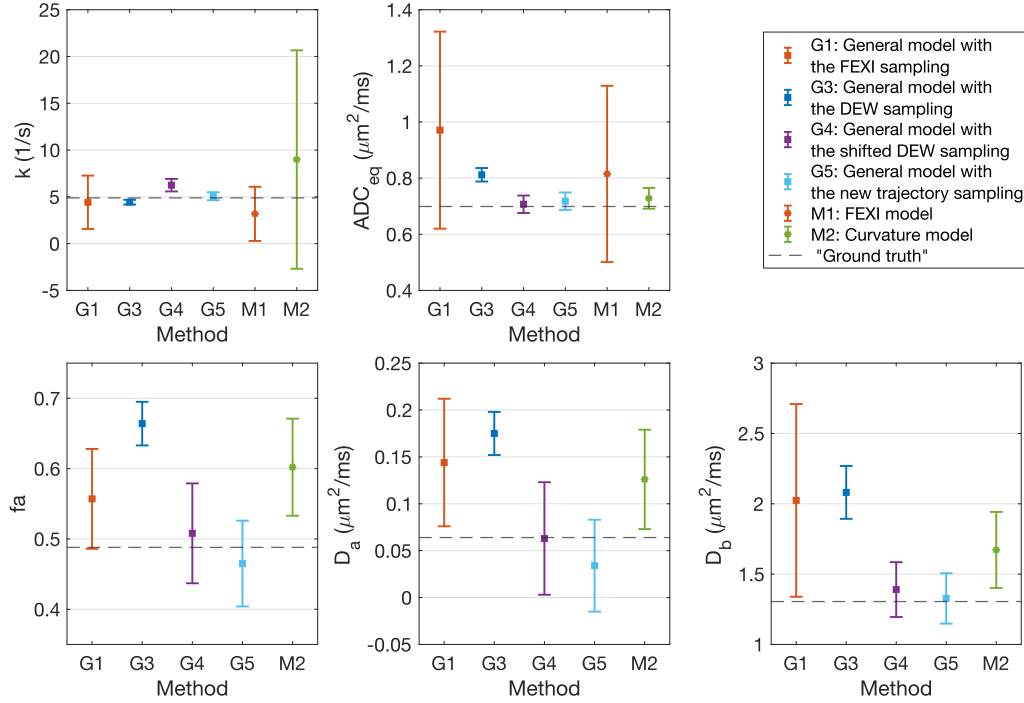
Figure 4.10: Error bar plots of the exchange parameters estimated using the models under free diffusion assumptions for ROI. Points and the error bars represent means and standard deviations of the estimates, respectively. The "ground truths" are plotted with dashed gray lines for comparison. The estimates from the general model with the curvature subsampling scheme are not presented since they greatly deviate from the "ground truths".

The results obtained using the general model with different subsampled datasets are relatively consistent except for the curvature dataset. The shifted DEW and new trajectory sampling schemes performed well. The new trajectory sampling yielded a k closest to the one from the full space sampling and an ADC_{eq} almost identical to the full space sampling one. The shifted DEW sampling gave the most consistent estimates of the diffusion coefficients with the full space sampling. However, the D_a obtained from the new trajectory sampling and the k from the shifted DEW sampling deviate from the full space ones. The estimates with the lowest voxel-to-voxel variance were given by the DEW sampling. This sampling scheme also provided a k close to the full space one, however, estimates of both D_a and D_b greatly deviate. The FEXI sampling gave a close value of k to the full space one but predicted much higher values of both D_a and D_b over the full space ones. Moreover, the estimates from the FEXI sampling exhibited prominent voxel-to-voxel variations. The curvature sampling performed worst, yielding very erratic results.

The FEXI model yielded an AXR about 35% lower than the full space sampling one and the estimated ADC_{eq} is higher. Similarly to the general estimation with the FEXI sampling, noticeable voxel-to-voxel variations also appear in the parameters obtained using the FEXI model.

Table 4.1: Exchange parameters obtained from each estimation method. The mean and the standard deviation (std) of each parameter for the ROI are shown as "mean ± std". Note that the ADC_{eq}, D_a, D_b and f_a in the curvature estimation were obtained using a bi-exponential diffusion decay model.

General model						
Dataset	k (1/s)	T_1 (ms)	ADC_{eq} (μm^2/ms)	D_a (μm^2/ms)	D_b (μm^2/ms)	f_a
Full space	4.888±0.183	227.9±0.6	0.699±0.011	0.064±0.015	1.305±0.049	0.488±0.018
FEXI	4.420±2.851	222.2±1.9	0.971±0.351	0.144±0.068	2.024±0.685	0.557±0.071
Curvature	242.9±89.5	229.8±2.2	0.570±0.052	$2.8\times10^{-4}\pm3.0\times10^{-4}$	1.439±0.296	0.584±0.114
DEW	4.434±0.253	226.6±1.4	0.812±0.024	0.175±0.023	2.081±0.188	0.664±0.031
Shifted DEW	6.247±0.669	233.7±1.5	0.707±0.031	0.063±0.060	1.390±0.195	0.508±0.071
New trajectory	5.066±0.431	233.5±1.3	0.718±0.031	0.034±0.049	1.327±0.179	0.465±0.061
FEXI and curvature models						
FEXI	AXR (1/s)	T_1 (ms)	ADC_{eq} (μm^2/ms)	σ		
	3.182±2.893	220.7±2.3	0.815±0.314	0.678±0.106		
Curvature	k (1/s)	α	ADC_{eq} (μm^2/ms)	D_a (μm^2/ms)	D_b (μm^2/ms)	f_a
	8.966±11.644	0.0024±0.0014	0.728±0.037	0.126±0.053	1.672±0.270	0.602 ±0.069
DEW model						
DEW	k (1/s)	T_1 (ms)	ADC_{eq} (μm^2/ms)	D_a (μm^2/ms)	D_b (μm^2/ms)	P_a
	18.378±0.672	300.0±5.9	0.698±0.016	0.428±0.013	1.097±0.044	0.597±0.012
	τ_a (ms)	τ_b (ms)				
	173.8±9.9	79.4±0.085				

The curvature model provided a k almost twice higher than the full space one and with an extremely large standard deviation between voxels. The estimated ADC_{eq} is consistent with the full space one, but both D_a and D_b deviate.

For the exchange parameters obtained using the DEW model, which assumes that the intra-cellular diffusion is restricted within a sphere, the DEW model yielded a much higher k than the parameters estimated under the free diffusion assumption. Although the estimate of D_a is much higher than the full space one and D_b is fairly lower, the fitted ADC_{eq} is nearly identical to the full space one.

The values of the MSRs of each model fitted to each dataset are given in table 4.2. All models fit the experimental data well except for the curvature sampling scheme in the two cases (the general and curvature models). The MSRs are around 0.002 for most fits. The lowest value for the MSR was obtained using the DEW model and the highest value was obtained by the fit of the curvature model. Similarly, the fits of DEW sampling with the general model yielded a relatively low MSR and the second highest MSR was obtained by the general model with the curvature sampling scheme. The fits of the FEXI sampling with both the general model and FEXI model perform well, giving fairly low MSRs. The fits of the new trajectory and shifted DEW datasets gave slightly higher MSRs.

Table 4.2: Mean squared residual of each estimation.

Estimation method	Mean squared residuals ($\times 10^{-3}$)					
	Used dataset					
	Full space	FEXI	Curvature	DEW	Shifted DEW	New trajectory
General model	1.99	1.76	4.81	2.19	2.44	2.93
FEXI model		1.88				
Curvature model			4.92			
DEW model				1.73		

5 Discussion

5.1 Results

For the acquired experimental data, the unexpected peaks observed in the 2D signal profile with $b_1 = b_2$ could be artifacts, as mentioned before. The peaks disturb the decay trend of the entire experimental dataset. In order to keep the accuracy of the estimates, the peaks were discarded from the full space and FEXI datasets. Excluding the peaks, the FEXI dataset still has 13 samples for each t_m, fulfilling the criteria for a fair comparison. The curvature, shifted DEW and new trajectory samplings were designed to avoid using the peaks. For example, the number of the subsampled dataset for each t_m was set as an even number (14), enabling the curvature trajectory not to pass through the peaks.

The estimates from the full space dataset are fairly close to the parameters reported in the previous studies [9, 10]. The slight variations can be caused by the different experimental procedures, such as the MR scanner and sample preparations. Moreover, the estimates presented very low voxel-to-voxel variances and the fit yielded relatively low residuals. The performance of the full space estimations suggests their adequacy to be used as "ground truths" for the estimates obtained from the subsampling schemes and data reduction frameworks (except for the DEW model).

The new trajectory and shifted DEW sampling schemes performed better than the other sampling schemes and the data reduction methods (i.e., the FEXI and curvature models), yielding estimates most consistent with the "ground truths" and with low voxel-to-voxel variations. Their good performance could be explained by the fact that both the datasets sampled using the two schemes are able to present the primary decay trend of the full space dataset. That is to say, the two subsampled datasets contain samples with increasing values of both b_1 and b_2. With the employed range of *b-values*, the signal intensity for each t_m can attenuate to approximately 50%. This could help the fitting process to effectively distinguish the intra- and extracellular components, and thus better estimate the exchange parameters. Moreover, the experimental data of the two sampling schemes have generally adequate SNR, helping retain the accuracy of estimates from the two schemes. The two schemes yielded consistent extracellular (fast) diffusion coefficients but different intracellular (slow) diffusion coefficients, this

could be attributed to that the experimental data with low values of b_1 and b_2 have a relatively higher SNR than the data with large b_1 and b_2. With regard to the DEW sampling scheme, whose data also exhibit the main decay trend, is expected to provide consistent parameters with the "ground truths" when analyzing its data using the general model. However, the artifact peaks affected the estimates from the DEW sampling, leading to deviations of both the diffusion coefficients.

For the FEXI sampling, although the fits of its dataset with both the general and FEXI models provided low residuals, the estimates obtained from both models deviated from the "ground truths" and presented prominent voxel-to-voxel variations. These deviations and variations could be due to the employed b_1 and the range of b_2. As previously discussed, the SNR of the data with a high *b-value* could decline to an extent. The FEXI data were sampled with the highest b_1 and could be noisier. Besides, the signal decayed only 25% for even the longest t_m, resulting in the intra- and extracellular contributions being difficult to be separated. Thus, the data without an adequate SNR and intensity attenuation affected the accuracy of the estimates from the FEXI sampling.

For the curvature dataset, the fits obtained using both the general and curvature models failed to yield reasonable estimates and presented the highest and second-highest residuals over the other fits. The general model performed worst, yielding erratic parameters. This unsatisfactory performance could be due to the minor differences in signal intensities between the experimental data, and thus, the general model failed to fit the data. Similarly, the accuracy of the estimates from the curvature model also depends on the difference in the signal intensities between data points, specifically, the curvature of the experimental data. The curvature degree of the experimental data is rather shallow. Minor random variations between the experimental data would disturb an apparent curvature to be presented, resulting in incorrect estimation of the curvatures and consequently yielding inaccurate estimates of the exchange parameters. Although the curvature model failed to provide acceptable estimates of the experimental data, it yielded adequate estimation of the simulated data (with only three data points per t_m), as presented in section 4.2, suggesting the feasibility of measuring exchange using the curvature framework on the data without noise.

In the original curvature experiment, b_s was optimized to achieve the greatest curve depth (equation 2.54). However, the value of optimized b_s exceeded the range of *b-values* in this thesis work and would generate signal with an even lower SNR. Therefore, the optimization of b_s was not employed in this study. Moreover, the success of the original curvature experiment could be associated with its acquisition hardware and stable phantom. The original curvature experiment was performed on a 7-T MR scanner [11] with a much higher magnetic field strength than the MR scanner (0.55 T) employed in this study. Furthermore, the phantom used in the original experiment was a water-glass capillary array [11], which provided more stability than the yeast phantom, reducing the possibility of yielding the random variations in the results. Consequently, the signal measured in the original curvature experiment is with a considerably greater SNR and is able to provide clear curvatures for estimating exchange.

The DEW framework provided the estimates under the assumption that diffusion is not free within cells. The apparent intracellular diffusion coefficient obtained by this model could be closer to the intrinsic one since in reality, diffusion within a cell is restricted. On the contrary, the diffusion hindrance within a cell is not considered in the free diffusion assumption, leading to the estimated intracellular diffusion coefficient from the general model being lower than the intrinsic one.

Recalling the theory of the DEW framework presented in section 2.3, the expression of the initial condition for the signal intensity of the intracellular compartment is based on a long time limit condition (i.e., $\Delta \gg r^2/D_a$). However, this condition is not met in this thesis since

this work primarily studies the exchange measurements using the general and general-based models (i.e., the FEXI and curvature models), in which exchange is assumed to occur only during the mixing time but not the diffusion time (Δ). Thus, a short Δ was applied in this study, consequently affecting the accuracy of the estimates from the DEW model.

5.2 Method

The models employed in this study, except for the DEW one, are based on the free diffusion assumption. However, in living tissues, diffusion is hindered by obstacles such as macro-molecules and cell membranes. Thus, free diffusion is no longer accurate in describing this restricted motion of molecules in living tissues, which could be seen as a limitation of the free-diffusion-based models. The DEW framework accounts for the geometry of a cell and models it as a sphere restricting intracellular diffusion. This model could provide estimates of diffusion and exchange parameters closer to their intrinsic ones as discussed before. Living tissues are complex and the mechanisms controlling the diffusion and water exchange in tissues remain unclear. Although the assumption-based models deviate from reality, they allow analytical calculation of the MR signal attenuation resulting from the diffusion and exchange process and still provide significant insights into the diffusion and exchange mechanisms in tissues.

As previously mentioned, the general and general-based models neglect exchange during the applications of diffusion encoding, but water exchange continuously occurs, resulting in the exchanging population during the diffusion blocks being unconsidered. Furthermore, for all the models, relaxation times (T_1 and T_2) are assumed to be the same (or very similar) for both compartments. However, in reality, relaxation times in different compartments are not identical. For long t_m and TE, the difference in signal attenuation rates of each compartment due to relaxation is prominent. This difference would affect the accuracy of the estimates for diffusion and exchange parameters. Although these two assumptions introduce unavoidable errors in the estimation, they simplify the mathematical analysis of the exchange process. Considering exchange during the diffusion encodings and different relaxation rates for the two compartments would make the exchange process analytically intractable.

The acquisition parameters selected in this study is a compromise between achieving the experimental purposes and reducing the errors in the estimates due to these assumptions. As previously mentioned, a small value of Δ (i.e., $\Delta \ll 1/k$) was chosen to minimize the exchange effect during diffusion encodings. A short δ was selected for the same purpose. The mean residence time ($1/k$) is on the time scale of 200 - 300 ms according to a literature value for k [9]. Besides, in order to better separate the components of the two compartments of the signal attenuation, the difference between intra- and extracellular diffusion coefficients needs to be enhanced. Previous studies have shown that the effect of cell hindrance displays as a decreasing apparent intracellular diffusion coefficient with increasing Δ and δ [45]. The time scale for the apparent intracellular diffusion coefficient to display the restricted effect is 1 ms [9]. The value of Δ was set as 10 ms to compromise these two purposes, minimizing the influence of exchange during diffusion encodings and maximizing the difference between intra- and extracellular diffusion coefficients. Similarly, the value of δ was also chosen between the two time scales, but much lower than Δ ($\delta = 1.5$ ms), since the SGP approximation in the DEW framework was also considered.

Furthermore, although a long t_m can introduce more weighting of exchanging, large values of t_m will enhance the effect of T_1-relaxation during t_m. As discussed above, this effect leads to errors in estimates when T_1 relaxation times of the two compartments are not equal. Thus, an upper limit in the range of t_m was set to reduce the effect of T_1-relaxation during t_m. A limited t_m can also reduce signal attenuation leading to lower SNR. Likewise, a small value of TE was

chosen to limit the effect of T_2 relaxation during the two PGSE blocks, thus diminishing the estimation errors and improving SNR.

For the acquisition sequence, a pair of spoiler gradients was used in this study to suppress the undesired signal produced by the second pair of 90°-180° RF pulses. The amplitude of the spoiler gradients was adjusted roughly by observing the intensity of the detected signal. One may result in the acquired signal not purely from the stimulated echo. An experimental method can be applied to optimize the design of spoiler gradients [8]. This can be achieved by using the original sequence without the first 90° RF pulse and experimentally tuning the amplitude of spoilers. The value of the amplitude is chosen until no signal created by the second pair of 90°-180° RF pulses is observed. However, it would be time-consuming to exclude the first 90° RF pulse from the original sequence using openMATLAB. Due to time limitations, this optimization procedure was not implemented in this study.

An alternative way to only select the desired stimulated echo is phase cycling [8], in which the sequence is repeated several times (in an even number) and the phases of the RF pulses vary in a designed manner for each repetition. By averaging the sum of the repetitions, the unwanted signal is canceled and the desired signal (i.e., the stimulated echo signal in this study) is kept. Although phase cycling requires more acquisition time, it is worth exploring since this method is inherently more effective in suppressing the unwanted signal than using spoilers [46]. Moreover, unlike spoiler gradients, phase cycling will not introduce estimation errors due to additional diffusion weighting caused by the application of gradients.

For the total acquisition time, it was unexpectedly longer than the designed one. The exchange measurement took almost 14 hours. However, the total acquisition time should be less than 6 hours in accordance with the time parameters selected in this study. The time length of the break between repetitions of the sequence increased randomly during the scan. This problem in the implemented sequence script was not solved due to the limited time of this thesis work. However, it is crucial to shortening the scan time when implementing experiments on yeast cell suspensions. Yeast phantom is unstable and will produce carbon dioxide from time to time. The longer the yeast phantom is scanned, the more likely it will release bubbles during the scan, thus affecting the measured data. Furthermore, fast acquisition methods, such as fast spin-echo and echo-planar imaging, can be explored to be implemented on the benchtop MR scanner to further shorten the acquisition time. On the other hand, fast acquisition enable an increase in the number of averages to improve SNR.

Anisotropy effects are not considered in the exchange models employed in this study. However, diffusion and water exchange are orientation-dependent in anisotropic media. A previous study [47] has suggested that the exchange rate in human white matter is affected by the different diffusion-encoding directions. Thus, further studies could focus on introducing anisotropy to the exchange models. Besides, this work is limited to a two-compartment exchange system and steady-state exchange is assumed in most exchange models. The frameworks could be further generalized for multi-compartment and non-steady-state exchange.

6 Conclusion

A DEXSY experiment was successfully implemented on a benchtop MR scanner to acquire a 2D dataset. The acquired dataset was subsampled based on three existing frameworks, the FEXI, curvature and DEW models, and two alternative subsampling schemes proposed in this work, the shifted DEW and new trajectory schemes. The subsampled datasets were analyzed using the three frameworks and a general model. The estimates from the full space dataset using the general model were employed as "ground truths" to assess the results from the general model with different subsampling schemes, FEXI and curvature models.

The results suggest the feasibility of various schemes for subsampling the 2D dataset acquired using the benchtop MR scanner for estimating water exchange. All the methods except the curvature sampling scheme employed using both the general and curvature models provided reasonable estimates. With a similar number and range of *b-values*, shifted DEW and new trajectory sampling schemes performed better over others in terms of consistency with the "ground truths" and low variations between voxels, suggesting they are worth further study and optimization to measure exchange. The DEW sampling with the general model yielded diffusion coefficients that deviated probably due to the peak artifacts. The FEXI sampling with both its own and the general models gave estimates that deviated from the "ground truths" and were with prominent standard deviations due to the inadequate SNR and range of *b-values*. The curvature dataset analyzed with both the curvature and general models failed to provide reasonable estimates since the success of these methods requires a fairly high SNR. The DEW model provided information for restricted diffusion, but "ground truth" was lacking to assess the estimates from this model.

Bibliography

[1] G. Benga. "Water transport red blood cell membranes". In: *Progress in Biophysics and Molecular Biology* 51.3 (1988), pp. 193–245. ISSN: 0079-6107. DOI: https://doi.org/10.1016/0079-6107(88)90002-8.

[2] M. Amiry-Moghaddam and O. P. Ottersen. "The molecular basis of water transport in the brain". In: *Nature Reviews Neuroscience* 4.12 (1 Dec. 2003), pp. 991–1001. ISSN: 1471-003X. DOI: https://doi.org/10.1038/nrn1252.

[3] J. Brahm. "Urea permeability of human red cells". In: *The Journal of general physiology* 82.1 (1 July 1983), pp. 1–23. ISSN: 0022-1295. DOI: https://doi.org/10.1085/jgp.82.1.1.

[4] J. Hu and A. S. Verkman. "Increased migration and metastatic potential of tumor cells expressing aquaporin water channels". In: *The FASEB Journal* 20.11 (1 Sept. 2006), pp. 1892–1894. DOI: https://doi.org/10.1096/fj.06-5930fje.

[5] M. J. Volles and P. T. Lansbury. "Vesicle Permeabilization by Protofibrillar -Synuclein Is Sensitive to Parkinson's Disease-Linked Mutations and Occurs by a Pore-like Mechanism". In: *Biochemistry* 41.14 (15 Mar. 2002), pp. 4595–4602. ISSN: 0006-2960. DOI: https://doi.org/10.1021/bi0121353.

[6] P. T. Callaghan and I. Furó. "Diffusion-diffusion correlation and exchange as a signature for local order and dynamics". In: *The Journal of Chemical Physics* 120.8 (20 Feb. 2004), pp. 4032–4038. ISSN: 0021-9606. DOI: https://doi.org/10.1063/1.1642604.

[7] S. Ramadan and C. E. Mountford. "Diffusion Exchange Weighted (DEW) imaging". In: *International Society for Magnetic Resonance in Medicine Annual Meeting and Exhibition* (May 6–12, 2006).

[8] S. Ramadan. "Diffusion-Exchange Weighted Imaging". In: *Magnetic Resonance Insights* 3 (9 Nov. 2009), MRI.S3504. DOI: https://doi.org/10.4137/MRI.S3504.

[9] I. Åslund, A. Nowacka, M. Nilsson, and D. Topgaard. "Filter-exchange PGSE NMR determination of cell membrane permeability." In: *Journal of Magnetic Resonance* 200 (Oct. 2009), pp. 291–295. ISSN: 1096-0856. DOI: https://doi.org/10.1016/j.jmr.2009.07.015.

[10]   S. Lasič, M. Nilsson, J. Lätt, F. Ståhlberg, and D. Topgaard. "Apparent exchange rate mapping with diffusion MRI". In: *Magnetic Resonance in Medicine* 66.2 (28 Mar. 2011), pp. 356–365. DOI: `https://doi.org/10.1002/mrm.22782`.

[11]   T. X. Cai, D. Benjamini, M. E. Komlosh, P. J. Basser, and N. H. Williamson. "Rapid detection of the presence of diffusion exchange". In: *Journal of Magnetic Resonance* 297 (Dec. 2018), pp. 17–22. ISSN: 1090-7807. DOI: `https://doi.org/10.1016/j.jmr.2018.10.004`.

[12]   M. Nilsson, J. Lätt, D. Van Westen, S. Brockstedt, S. Lasič, F. Ståhlberg, and D. Topgaard. "Noninvasive mapping of water diffusional exchange in the human brain using filter-exchange imaging". In: *Magnetic Resonance in Medicine* 69.6 (26 July 2013), pp. 1572–1580. DOI: `https://doi.org/10.1002/mrm.24395`.

[13]   S. Lasič, S. Oredsson, S. C. Partridge, L. H. Saal, D. Topgaard, M. Nilsson, and K. Bryskhe. "Apparent exchange rate for breast cancer characterization". In: *NMR in Biomedicine* 29.5 (29 Feb. 2016), pp. 631–639. DOI: `https://doi.org/10.1002/nbm.3504`.

[14]   R. W. Brown, Y. C. N. Cheng, E. M. Haacke, M. R. Thompson, and R. Venkatesan. *Magnetic Resonance Imaging: Physical Principles and Sequence Design*. 2nd ed. John Wiley & Sons, Ltd, Apr. 2014. ISBN: 978-1118633977. DOI: `https://doi.org/10.1002/9781118633953.fmatter`.

[15]   P. J. Basser and E. Özarslan. "Introduction to Diffusion MR". In: *Diffusion MRI: From Quantitative Measurement to In-vivo Neuroanatomy*. Ed. by H. Johansen-Berg and T.E.J. Behrens. Elsevier/Academic Press, 2014. ISBN: 978-0123747099. DOI: `https://doi.org/10.1016/C2011-0-07047-3`.

[16]   R. Brown. "XXVII. A brief account of microscopical observations made in the months of June, July and August 1827, on the particles contained in the pollen of plants; and on the general existence of active molecules in organic and inorganic bodies". In: *The Philosophical Magazine* 4.21 (1828), pp. 161–173. DOI: `https://doi.org/10.1080/14786442808674769`.

[17]   A. Einstein. "Über die von der molekularkinetischen Theorie der Wärme geforderte Bewegung von in ruhenden Flüssigkeiten suspendierten Teilchen". In: *Annalen der Physik* 322.8 (1905), pp. 549–560. DOI: `https://doi.org/10.1002/andp.19053220806`.

[18]   J. Topping. "Investigations on the Theory of the Brownian Movement". In: *Physics Bulletin* 7.10 (Oct. 1956). DOI: `https://doi.org/10.1088/0031-9112/7/10/012`.

[19]   E. L. Hahn. "Spin Echoes". In: *Phys. Rev.* 80 (4 Nov. 1950), pp. 580–594. DOI: `https://doi.org/10.1103/PhysRev.80.580`.

[20]   H. Y. Carr and E. M. Purcell. "Effects of Diffusion on Free Precession in Nuclear Magnetic Resonance Experiments". In: *Phys. Rev.* 94.0 (3 May 1954), pp. 630–638. DOI: `https://doi.org/10.1103/PhysRev.94.630`.

[21]   E. O. Stejskal and J. E. Tanner. "Spin Diffusion Measurements: Spin Echoes in the Presence of a Time-Dependent Field Gradient". In: *The Journal of Chemical Physics* 42.1 (20 July 1965), pp. 288–292. DOI: `https://doi.org/10.1063/1.1695690`.

[22]   C. F. Westin, H. Knutsson, O. Pasternak, F. Szczepankiewicz, E. Özarslan, D. Van Westen, C. Mattisson, M. Bogren, L. J. O'Donnell, M. Kubicki, and et al. "Q-space trajectory imaging for multidimensional diffusion MRI of the human brain". In: *NeuroImage* 135 (15 July 2016), pp. 345–362. ISSN: 1053-8119. DOI: `https://doi.org/10.1016/j.neuroimage.2016.02.039`.

[23] J. Mattiello, P. J. Basser, and D. Le Bihan. "Analytical Expressions for the b Matrix in NMR Diffusion Imaging and Spectroscopy". In: *Journal of Magnetic Resonance, Series A* 108.2 (June 1994), pp. 131–141. ISSN: 1064-1858. DOI: https://doi.org/10.1006/jmra.1994.1103.

[24] D. Le Bihan. "Magnetic Resonance Diffusion Imaging: Introduction and Concepts". In: *Diffusion MRI: Theory, Methods, and Applications*. Ed. by D. K. Jones. Oxford, UK: Oxford University Press, Sept. 2012. ISBN: 978-0199965144. DOI: https://doi.org/10.1093/med/9780195369779.001.0001.

[25] D. Le Bihan. "Looking into the functional architecture of the brain with diffusion MRI". In: *Nature reviews. Neuroscience* 4.6 (1 June 2003), pp. 469–480. ISSN: 1471-003X. DOI: https://doi.org/10.1038/nrn1119.

[26] P. J. Basser, J. Mattiello, and D. Le Bihan. "MR diffusion tensor spectroscopy and imaging." In: *Biophysical Journal* 66 (Jan. 1994), pp. 259–267. ISSN: 1542-0086. DOI: https://doi.org/10.1016/S0006-3495(94)80775-1.

[27] R. M. Henkelman, G. J. Stanisz, J. K. Kim, and M. J. Bronskill. "Anisotropy of NMR properties of tissues". In: *Magnetic Resonance in Medicine* 32.5 (Nov. 1994), pp. 592–601. ISSN: 0740-3194. DOI: https://doi.org/10.1002/mrm.1910320508.

[28] P. J. Basser. "Inferring microstructural features and the physiological state of tissues from diffusion-weighted images". In: *NMR in Biomedicine* 8.7 (Dec. 1995), pp. 333–344. DOI: https://doi.org/10.1002/nbm.1940080707.

[29] A. V. Barzykin, K. Hayamizu, W. S. Price, and M. Tachiya. "Pulsed-Field-Gradient NMR of Diffusive Transport through a Spherical Interface into an External Medium Containing a Relaxation Agent". In: *Journal of Magnetic Resonance, Series A* 114.1 (May 1995), pp. 39–46. ISSN: 1064-1858. DOI: https://doi.org/10.1006/jmra.1995.1103.

[30] J. Kärger. "NMR self-diffusion studies in heterogeneous systems". In: *Advances in Colloid and Interface Science* 23 (Aug. 1985), pp. 129–148. ISSN: 0001-8686. DOI: https://doi.org/10.1016/0001-8686(85)80018-X.

[31] W. S. Price, A. V. Barzykin, K. Hayamizu, and M. Tachiya. "A Model for Diffusive Transport through a Spherical Interface Probed by Pulsed-Field Gradient NMR". In: *Biophysical Journal* 74.5 (1 May 1998), pp. 2259–2271. ISSN: 0006-3495. DOI: https://doi.org/10.1016/S0006-3495(98)77935-4.

[32] Y. Q. Song, L. Venkataramanan, M. D. Hürlimann, M. Flaum, P. Frulla, and C. Straley. "T1–T2 Correlation Spectra Obtained Using a Fast Two-Dimensional Laplace Inversion". In: *Journal of Magnetic Resonance* 154.2 (Feb. 2002), pp. 261–268. ISSN: 1090-7807. DOI: https://doi.org/10.1006/jmre.2001.2474.

[33] K. E. Washburn and P. T. Callaghan. "Tracking Pore to Pore Exchange Using Relaxation Exchange Spectroscopy". In: *Physical Review Letters* 97 (17 Oct. 2006), p. 175502. ISSN: 1090-7807. DOI: https://doi.org/10.1103/PhysRevLett.97.175502.

[34] G. N. Lewis. "A New Principle of Equilibrium". In: *Proceedings of the National Academy of Sciences* 11.3 (1 Mar. 1925), pp. 179–183. ISSN: 0027-8424. DOI: https://doi.org/10.1073/pnas.11.3.179.

[35] J. E. House. *Principles of chemical kinetics*. 2nd ed. Academic press, 2007. ISBN: 978-0123567871.

[36] R. J. LeVeque. *Finite difference methods for ordinary and partial differential equations*. Steady State and Time Dependent Problems. SIAM, 2007. ISBN: 978-0898716290. DOI: http://dx.doi.org/10.1137/1.9780898717839.

[37] N. H. Williamson, R. Ravin, T. X. Cai, D. Benjamini, M. Falgairolle, M. J. O'Donovan, and P. J. Basser. "Real-time measurement of diffusion exchange rate in biological tissue". In: *Journal of Magnetic Resonance* 317 (Aug. 2020), p. 106782. ISSN: 1090-7807. DOI: https://doi.org/10.1016/j.jmr.2020.106782.

[38] E. Fieremans and H. H. Lee. "Physical and numerical phantoms for the validation of brain microstructural MRI: A cookbook". In: *NeuroImage* 182 (15 Nov. 2018), pp. 39–61. ISSN: 1053-8119. DOI: https://doi.org/10.1016/j.neuroimage.2018.06.046.

[39] N. Moutal, M. Nilsson, D. Topgaard, and D. Grebenkov. "The Kärger vs bi-exponential model: theoretical insights and experimental validations". In: *Journal of Magnetic Resonance* 296 (Nov. 2018), pp. 72–78. ISSN: 1090-7807. DOI: https://doi.org/10.1016/j.jmr.2018.08.015.

[40] Pure Devices. *Research Lab, Drive L, Detailed Specifications*. Pure Devices GmbH. Rimpar, Germany, 2019.

[41] Pure Devices. *magspec, Permament magnet, Device Instruction Manual*. Pure Devices GmbH. Rimpar, Germany, 2017.

[42] Pure Devices. *DC-600, High-Power Gradient Amplifier, Device Instruction Manual*. Pure Devices GmbH. Rimpar, Germany, 2019.

[43] R. C. Gonzalez and R. E. Woods. *Digital Image Processing, Global Edition*. 4th ed. Pearson, 2018. ISBN: 978-1292223049.

[44] A. Ordinola. "MRI based measurement of diffusion and water exchange - Study with a benchtop MR scanner". MA thesis. Linköping University, Linköping, Sweden, June 2021.

[45] I. Åslund and D. Topgaard. "Determination of the self-diffusion coefficient of intracellular water using PGSE NMR with variable gradient pulse length". In: *Journal of Magnetic Resonance* 201.2 (Dec. 2009), pp. 250–254. ISSN: 1090-7807. DOI: https://doi.org/10.1016/j.jmr.2009.09.006.

[46] J.C. Lindon. "NUCLEAR MAGNETIC RESONANCE SPECTROSCOPY TECHNIQUES | Multidimensional Proton". In: *Encyclopedia of Analytical Science*. Ed. by P. Worsfold, A. Townshend, and C. Poole. 2nd ed. Oxford: Elsevier, 2005, pp. 350–357. ISBN: 978-0123693976. DOI: https://doi.org/10.1016/B0-12-369397-7/00413-1.

[47] Z. Li, Z. Pang, J. Cheng, Y. C. Hsu, Y. Sun, E. Özarslan, and R. Bai. "The direction-dependence of apparent water exchange rate in human white matter". In: *NeuroImage* 247 (15 Feb. 2022), p. 118831. ISSN: 1053-8119. DOI: https://doi.org/10.1016/j.neuroimage.2021.118831.